PSFC/JA-24-47

Stability and Transport of Gyrokinetic Critical Pedestals

Jason Parisi[1], Andrew Oakleigh Nelson[2], Walter Guttenfelder[3], Rahul Gaur[4], John W Berkery[5], Stanley M Kaye[6], Kshitish Kumar Barada[7], Cesar F Clauser[8], Ahmed Diallo[9], David R Hatch[10], Andreas Kleiner[11], Mate Lampert[1], Tanmay Macwan[12] and Jonathan E Menard[13]

[1] Princeton Plasma Physics Laboratory, Princeton, New Jersey, UNITED STATES
[2] Applied Physics and Applied Mathematics, Columbia University, 500 W 120th St, New York, New York, 10027-6902, UNITED STATES
[3] Princeton Plasma Physics Laboratory, Princeton, NJ 08543, USA, Princeton, New Jersey, 08540, UNITED STATES
[4] Physics, University of Maryland at College Park, College Park, Maryland, 20742-5031, UNITED STATES
[5] Princeton University Plasma Physics Laboratory, Princeton, NJ 08543, Princeton, New Jersey, 08543, UNITED STATES
[6] Princeton Plasma Physics Laboratory, James Forrestal Campus, PO Box 451, Princeton, NJ 08543-0451, USA, Princeton, New Jersey, 08543, UNITED STATES
[7] UCLA, Los Angeles, California, UNITED STATES
[8] Massachusetts Institute of Technology Plasma Science and Fusion Center, Cambridge, Massachusetts, UNITED STATES
[9] Plasma Physics Laboratory, Princeton University Plasma Physics Laboratory, Princeton, NJ 08544, USA, Princeton, New Jersey, 08543-0451, UNITED STATES
[10] Institute for Fusion Studies, University of Texas at Austin, Austin, Texas, UNITED STATES
[11] Theory, Princeton University Plasma Physics Laboratory, P.O. Box 451, Princeton, New Jersey, 08543-0451, UNITED STATES
[12] Department of Physics and Astronomy, University of California Los Angeles, 475 Portola Plaza, Los Angeles, Los Angeles, California, 90095, UNITED STATES
[13] NSTX Upgrade, Princeton Plasma Physics Laboratory, P.O. Box 451, Princeton, New Jersey, 08543, UNITED STATES

January 2024

Plasma Science and Fusion Center
Massachusetts Institute of Technology
Cambridge MA 02139 USA

This work was supported by the U.S. DoE under contract numbers DE-AC02-09CH11466, DE-SC0022270, DESC0022272, and the DoE Early Career Research Program.

Submitted to *Nuclear Fusion*

Stability and Transport of Gyrokinetic Critical Pedestals

J. F. Parisi[1,*], A. O. Nelson[2], W. Guttenfelder[3,1], R. Gaur[4], J. W. Berkery[1], S. M. Kaye[1], K. Barada[5], C. Clauser[6], A. Diallo[1], D. R. Hatch[7,8], A. Kleiner[1], M. Lampert[1], T. Macwan[5], and J. E. Menard[1]

[1]Princeton Plasma Physics Laboratory, Princeton University, Princeton, NJ, USA
[2]Department of Applied Physics and Applied Mathematics, Columbia University, New York, NY, USA
[3]Type One Energy, 8383 Greenway Boulevard, Middleton, WI, USA
[4]Department of Mechanical and Aerospace Engineering, Princeton University, Princeton, NJ, USA
[5]University of California, Los Angeles, Los Angeles, CA, USA
[6]Plasma Science and Fusion Center, Massachusetts Institute of Technology, Cambridge, MA, USA
[7]Institute for Fusion Studies, University of Texas at Austin, Austin, Texas, USA
[8]ExoFusion, Austin, Texas, USA

*Email: jparisi@pppl.gov

Abstract

A gyrokinetic threshold model for pedestal width-height scaling prediction is applied to multiple devices. A shaping and aspect-ratio scan is performed on NSTX equilibria, finding $\Delta_{\rm ped} = 0.92 A^{1.04} \kappa^{-1.24} 0.38^{\delta} \beta_{\theta,{\rm ped}}^{1.05}$ for the wide-pedestal branch with pedestal width $\Delta_{\rm ped}$, aspect-ratio A, elongation κ, triangularity δ, and normalized pedestal height $\beta_{\theta,{\rm ped}}$. A width-transport scaling is found to vary significantly if pedestal height is varied either with fixed density or fixed temperature, showing how fueling and heating sources affect the pedestal density and temperature profiles for the kinetic-ballooning-mode (KBM) limited profiles. For an NSTX equilibrium, at fixed density, the wide-branch is $\Delta_{\rm ped} = 0.028\,(q_e/\Gamma_e - 1.7)^{1.5} \sim \eta_e^{1.5}$ and at fixed temperature $\Delta_{\rm ped} = 0.31\,(q_e/\Gamma_e - 4.7)^{0.85} \sim \eta_e^{0.85}$ where q_e and Γ_e are turbulent electron heat and particle fluxes and $\eta_e = \nabla \ln T_e / \nabla \ln n_e$ for electron temperature T_e and density n_e. Pedestals close to the KBM limit are shown to have modified turbulent transport coefficients compared to strongly driven KBMs. The role of flow-shear is studied as a width-height scaling constraint and pedestal saturation mechanism for a standard and lithiated wide pedestal discharge. Finally, the stability, transport, and flow-shear constraints are combined and examined for a NSTX experiment.

1 Introduction

The H-mode pedestal is an edge transport barrier that forms when a strongly heated tokamak plasma transitions into a high confinement regime [1, 2]. Due to significant improvements in confinement, H-mode is a leading candidate for burning plasma scenarios [3–6]. The pedestal pressure profile typically has a characteristic width and height [7], which can be determined with the EPED stability threshold model [8], often with remarkable success [5, 9–12] and some exceptions [13, 14]. EPED combines a local gradient constraint controlled by kinetic-ballooning-mode (KBM) stability (in practice calculated by the infinite-n ideal-ballooning-mode (IBM) [15] stability threshold, which was demonstrated to be close to the KBM threshold for a DIII-D pedestal [16], although several physics effects such as collisions and parallel magnetic field oscillations were absent for the KBM calculation) and a macroscopic stability constraint given by peeling-ballooning-mode (PBM) stability [17]. The intersection of KBM and PBM constraints gives a pedestal width-height prediction.

However, extra information from pedestal models is required in order to understand current experiments and design future devices [18, 19]. There is substantial experimental evidence [13, 20–25] that plasma shaping and aspect-ratio affect pedestal stability. The EPED model, originally developed for standard-aspect-ratio tokamaks with weak to moderate shaping [9], has been used to predict the effects of shaping on PBM stability [11, 26] with impressive experimental results [5], but it has not reported the effects of strong shaping or aspect-ratio on the KBM width-height scaling. EPED finds that KBM stability constrains the pedestal width $\Delta_{\rm ped}$ and height $\beta_{\theta,\rm ped}$ by $\Delta_{\rm ped} = G\beta_{\theta,\rm ped}^{1/2}$, where G typically has values of 0.07-0.10 for standard-aspect-ratio tokamaks, and G is assumed to be a weak function of shaping. Given that low-aspect-ratio devices often have strong plasma shaping [27], understanding how shaping and aspect-ratio enter the pedestal width-height scaling is an important step towards understanding current experiments and designing future devices.

While KBM and PBM stability might suffice to predict the pedestal pressure's width-height trajectory [28], the separate evolution of temperature and density pedestal profiles is also needed to determine plasma heating and fueling sources that are consistent with such profiles. Depending on the available heating and particle sources, certain pedestals may be inaccessible even if KBM and PBM stability analysis indicates they are stable. Given that gyrokinetic instabilities are often sensitive to density and/or temperature gradients and their relative sizes [29, 30], non-KBM transport mechanisms are also expected to play a significant role in pedestal evolution [16, 31–35]. Therefore, understanding how transport, sources, and stability are related is crucial for predictive pedestal models and future experimental capabilities.

Equilibrium flow-shear, part of which is generated by the temperature and density profiles themselves, is also reported to be important in pedestal formation in the L-H transition [36] and the inter-ELM cycle [37], and is hypothesized as necessary at the pedestal top to allow the pedestal to widen [8] by stabilizing ion-temperature-gradient and trapped-electron-mode instabilities. Given

the reported importance of flow-shear – and also its pessimistic scaling with $\rho_{*i} = \rho_i/a$ to future devices [38], where ρ_i is the ion gyroradius and a the minor radius – generating sufficient pedestal flow-shear in future reactors (or developing alternative methods [39]) is an important task. According to arguments in [38, 40], the ratio of the flow-shear rate γ_E to the typical linear growth rate γ scales as $\gamma_E/\gamma \sim (C_{\gamma_E}/C_\gamma)(a/\Delta_{\rm ped})\rho_{*i}$ where $\gamma_E = (\rho_i v_{th}/\Delta^2_{\rm ped})C_{\gamma_E}$ and $\gamma = (v_{th}/\Delta_{\rm ped})C_\gamma$. Here, $C_{\gamma_E} \sim 1$ and $C_\gamma = \gamma a/v_{th}$ are complicated functions, v_{th} is the thermal main ion speed, and $\Delta_{\rm ped}$ is the pedestal width. Notably, and of potential concern, experiments have found no strong dependence of $\Delta_{\rm ped}$ on ρ_{*i} [9, 41, 42]. Given that $\gamma_E/\gamma \gtrsim 1$ is an approximate condition for flow-shear suppression of microinstability, machines with better confinement ($\rho_{*i} \to 0$) may not have sufficient flow-shear for pedestal formation and/or high pedestal pressures because $\gamma_E/\gamma \ll 1$. There are also arguments [39] and experimental evidence [43, 44] for pedestal formation without requiring flow-shear due to the stabilizing effects of density gradients on microstability [29, 30, 45–47] and high Shafranov shift [48–50].

The pedestal is also highly coupled to the core and scrape-off layer (SOL) [51–53], meaning that the pedestal's evolution cannot be considered in isolation. Solving this coupling in sufficient detail remains one of the biggest challenges in fusion research [54] due in part to the high dimensionality of the problem, the complex interactions between phenomena, and the uncertainties in models and measurements. For example, predicting the pedestal density profile is a very hard problem. The density pedestal in current experiments is sensitive to both neutral particles ionizing in the pedestal after traveling through the SOL and transport processes in the pedestal [53, 55–59]. Changes in divertor and SOL physics and the neutral ionization source in the pedestal will change the pedestal pressure and current profile, in turn strongly affecting core physics, which in turns affects the pedestal, and so on.

In this work, we focus on three challenges mentioned above: (1) accuracy of the pedestal KBM width-height scaling across strong shaping and aspect-ratio, (2) pedestal heat and particle transport constraints, and (3) equilibrium flow-shear in the pedestal.

For (1), we introduce a linear gyrokinetic threshold model that builds on the EPED Ballooning Critical Pedestal model [9] to predict the width-height pedestal scaling across aspect-ratio, shaping, and devices. We call these Gyrokinetic Critical Pedestal width-height scaling expressions. We perform a study of how shaping and aspect-ratio enter the gyrokinetic pedestal width-height scaling, which may explain the differences in width-height experimental measurements between most devices and the National Spherical Torus Experiment (NSTX) [8, 13, 28], with NSTX typically featuring much wider pedestals. Varying the pedestal shaping and aspect-ratio may also provide new opportunities for controlling pedestal width and height in experiments. For (2), we study heat and particle transport around the gyrokinetic width-height scalings and find the dependence of pedestal width on the electron heat to particle transport ratio. We study how these width-transport scalings depend on whether the pedestal height is increased at fixed density or temperature, and across aspect-ratio. For

(3), we study flow-shear at the pedestal top in a regular NSTX ELMy H-mode and a NSTX ultra-wide enhanced pedestal (EP) H-mode [60].

The paper layout is as follows: in Section 2, we describe the process for varying the pedestal width and height with self-consistent equilibrium reconstruction. We introduce the gyrokinetic and ideal-ballooning framework used for studying these equilibria. A linear threshold model for gyrokinetic and ideal-ballooning stability is then applied to several devices in Section 3 to find width-height scaling expressions. The shaping and aspect-ratio dependence of the pedestal width-height-shaping scaling is explored in Section 4. In Section 5, we study gyrokinetic turbulent transport properties close to the Gyrokinetic Critical Pedestal boundaries and find scaling expressions that relate the pedestal width and turbulent transport ratios. We also show how these scaling expressions depend on plasma aspect-ratio and whether the pedestal height is increased at fixed temperature or fixed density. In Section 6 we explore the role of flow-shear as an additional width-height constraint. In Section 7, we combine the stability, flow-shear, and transport constraints to determine regions of pedestal width-height space that are accessible.

2 Width-Height Scaling Workflow

In this section, we describe the workflow to compute the width-height scaling using the new framework gk_ped, outlined in Figure 1. The primary purpose of gk_ped is to find the coefficients C and G of the pedestal width-height scaling expression $\Delta_{\mathrm{ped}} = C\left(\beta_{\theta,\mathrm{ped}}\right)^{G}$, where $\beta_{\theta,\mathrm{ped}}$ is the pedestal height (defined later in Equation (4)). Currently, gk_ped is implemented as a module in the integrated modeling and data analysis software OMFIT [61]. In addition to the OMFIT tools, we use EFIT-AI [62] combined with EFUND [63] for equilibrium reconstruction, GS2 [64, 65] and CGYRO [66] for gyrokinetic simulations, and BALOO [67] and ball_stab [65, 68] for infinite-n ballooning simulations.

As sketched in Figure 1, the general workflow is as follows: 1) An equilibrium (solution to the Grad-Shafranov equation) and profiles (temperature and density for all electrons and ion species) is input. The profiles are parameterized and fitted with a pedestal width Δ_{ped} and height $\beta_{\theta,\mathrm{ped}}$. 2) New equilibria and profiles are generated with varied pedestal width and height. The EFUND code is used to generate the Green's tables required for the free-boundary equilibrium reconstruction with EFIT. 3) The gyrokinetic and infinite-n stability properties of this set of equilibria are calculated with numerical calculations. Gyrokinetic stability is evaluated using GS2 and CGYRO, and infinite-n ballooning stability is evaluated using BALOO and ball_stab. 4) The pedestal width-height scaling expressions are found using the Gyrokinetic Critical Pedestal and Ballooning Critical Pedestal criteria, which use gyrokinetic and infinite-n simulation data. 5) These two criteria give width-height scaling expressions, output as $\Delta_{\mathrm{ped}} = C\left(\beta_{\theta,\mathrm{ped}}\right)^{G}$.

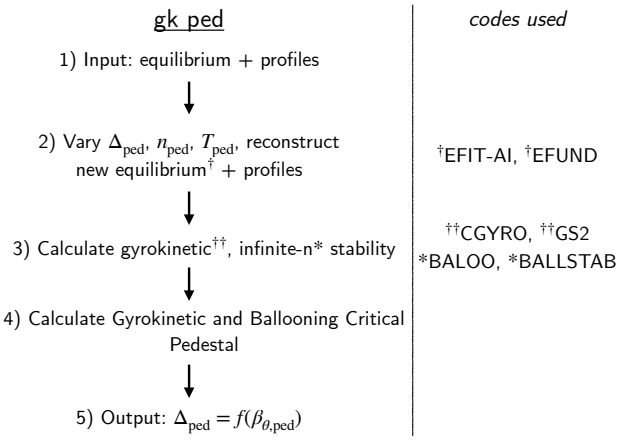

Figure 1: gk_ped workflow.

2.1 Equilibrium Variation and Reconstruction

The first step in gk_ped is to input an equilibrium and profiles. The input equilibrium and profiles are used to generate a set of equilibria and profiles where the pedestal width and height are varied self-consistently. In order to vary the pedestal width and height in a systematic manner, we parameterize the electron temperature and density profiles. The electron temperature is parameterized as

$$\begin{aligned} T_e(\psi) =& T_{e,\mathrm{c}} \mathrm{H}\left[\psi_{\mathrm{ped,T_e}} - \psi\right] \left(1 - \psi^{\alpha_{T_1}}\right)^{\alpha_{T_2}} \\ &+ T_{e0}\left(\tanh(2) - \tanh\left(\frac{\psi - \psi_{\mathrm{mid,T_e}}}{\Delta_{T_e}/2}\right)\right) + T_{\mathrm{e,sep}}, \end{aligned} \tag{1}$$

with the same functional form for electron density n_e [7, 8]. Here, H is a step function, ψ is the poloidal flux normalized to 0 at the magnetic axis and 1 at the last-closed-flux-surface, $T_{e,\mathrm{c}}$, T_{e0}, $\alpha_{T_{1,2}}$ are constants, Δ_{T_e} and Δ_{n_e} are the electron temperature and density pedestal widths. The pedestal heights $T_{e,\mathrm{ped}}$ and $n_{e,\mathrm{ped}}$ are $T_{e,\mathrm{ped}} = T_e(\psi_{\mathrm{ped,T_e}})$, $n_{e,\mathrm{ped}} = n(\psi_{\mathrm{ped,n_e}})$ where $T_{e,\mathrm{sep}}$ and $n_{e,\mathrm{sep}}$ are evaluated at $\psi = 1$, and $\psi_{\mathrm{ped,T_e}} = \psi_{\mathrm{mid,T_e}} - \Delta_{T_e}/2$, $\psi_{\mathrm{ped,n_e}} = \psi_{\mathrm{mid,n_e}} - \Delta_{n_e}/2$, For the ions, the density profiles are given by quasineutrality and the temperature profiles by enforcing constant T_i/T_e across the radial profile. After the input profiles are parameterized, the equilibrium is recalculated to ensure self-consistency. The current density $J(\psi)$ is the sum of bootstrap J_{bs} and non-bootstrap $J_{\mathrm{non-bs}}$ contributions,

$$J = J_{\mathrm{bs}} + kJ_{\mathrm{non-bs}}. \tag{2}$$

We vary the pedestal width and height with constant plasma current I_p, constant $\beta_N = \beta_T a B_{T0}/I_p$, and self-consistent bootstrap current. Here, $\beta_T = 8\pi\langle p\rangle_V/B_{T0}^2$, where $\langle p\rangle_V$ is the pressure averaged over the plasma volume and B_{T0} is the magnetic field strength at the magnetic axis. In order to keep I_p

constant due to changing $J_{\rm bs}$ resulting from different profiles, $J_{\rm non-bs}$ (obtained from the original input equilibrium), is multiplied by a constant k. The bootstrap current can be calculated from several formulae in the literature [69, 70] that are implemented in OMFIT, but is recommended that it be the same formula that generated the original input equilibrium. The quantity β_N is kept constant by an iterative procedure that allows β_N to vary from the input equilibrium by at most 1%.

Once the user is satisfied with the profile parameterization, the pedestal width and height are varied. The height can be varied in two ways: at constant $T_{e,\rm ped}$ with varying $n_{e,\rm ped}$, or at constant $n_{e,\rm ped}$ with varying $T_{e,\rm ped}$. As a default option, $n_{e,\rm ped}/n_{e,\rm sep}$ is held constant when varying $n_{e,\rm ped}$ and $T_{e,\rm sep}$ is held constant when varying $T_{e,\rm ped}$. The total pedestal width is

$$\Delta_{\rm ped} = (\Delta_{n_e} + \Delta_{T_e})/2, \tag{3}$$

the pedestal top location is $\psi_{\rm ped} = \psi_{\rm mid} - \Delta_{\rm ped}/2$ where $\psi_{\rm mid} = (\psi_{\rm mid,n_e} + \psi_{\rm mid,T_e})/2$, and the normalized pedestal height is

$$\beta_{\theta,\rm ped} = 8\pi p_{\rm ped}/\overline{B}^2_{\rm pol}, \tag{4}$$

where $p_{\rm ped} = 2p_e(\psi = \psi_{\rm ped})$ and $\overline{B}_{\rm pol} = 4\pi I_p/lc$ with flux surface circumference l and speed of light c [8, 28, 71].

2.2 Gyrokinetic and Ideal Analysis

In this section, we describe briefly the gyrokinetic and ideal simulations performed in the pedestal, and the gyrokinetic mode identification scheme.

We use GS2 [65] and CGYRO [66] to solve the electromagnetic gyrokinetic equation [72–75] for distribution function $g_s = \delta f_s + Z_s e F_{0s}(\phi - \chi)/T_s$,

$$\partial g_s/\partial t + \dot{\mathbf{R}}_{\mathbf{s}} \cdot \nabla \left[g_s + (Z_s e \chi_s/T_s)F_{0s}\right] + v_{\chi,s} \cdot \nabla F_{0s} - C_s = 0, \tag{5}$$

and Maxwell's equations. Here, δf_s is the total turbulent distribution function, F_{0s} is a Maxwellian, $\dot{\mathbf{R}}$ is the guiding-center particle drift, ϕ and χ_s are the electrostatic and gyroaveraged gyrokinetic potentials [75], $v_{\chi,s} = c\mathbf{B} \times \nabla\chi_s/B^2$, $\mathbf{B}$ is the magnetic field, and C_s is a collision operator. We also use BALOO [67] and ball_stab [65, 68] to solve the infinite-n ballooning equation for the ballooning eigenfunction Y and frequency ω [15], $\omega^2\lambda Y = -d/d\theta[g\ dY/d\theta] + uY$ where g, u, and λ are geometric coefficients [76]. We typically solve both ideal and gyrokinetic equations in the pedestal width-height model.

Linear gyrokinetic simulations are performed for a range of binormal wavenumbers k_y, typically at scales where kinetic-ballooning-modes (KBMs) [77, 78] are expected to be most virulent, i.e. $k_y\rho_i \approx 0.05 - 0.2$, and in a radial domain across the pedestal that is evenly spaced in ψ. Here, ρ_i is the ion gyroradius. Once simulations are converged, a mode finder routine adopting a fingerprints-like [56] approach is used to identify the mode type. To aid mode identification, each gyrokinetic simulation is launched with a second simulation with a

Table 1: Mode finder criteria in gk_ped. A '−' indicates that the quantity is not considered in the mode criterion.

Mode	χ_i/χ_e	D_e/χ_e	D_i/χ_i	$D_e/(\chi_e+\chi_i)$	$\mathcal{P}(A_\parallel)$	$\partial\gamma/\partial\beta$	ω_R
KBM	~ 1	~ 1	~ 1	$\gtrsim 1/3$	1	> 0	−
TEM	~ 1	~ 1	−	$\lesssim 1/3$	1	< 0	−
MTM	$\ll 1$	$\ll 1$	−	−	< 1	> 0	$\simeq \omega_{*e}$
ETG	$\ll 1$	$\ll 1$	−	−	1	−	−
TETG	$\ll 1$	$\ll 1$	−	−	< 1	−	−
ITG	$\gg 1$	−	$\ll 1$	−	1	< 0	−

slightly increased β value (where $d\beta/d\psi$ is unchanged) — this is particularly helpful for distinguishing between KBMs and trapped-electron-modes (TEMs) [79, 80], since both KBMs and TEMs often have similar transport characteristics [56, 81]. In Table 1, we describe the criteria for each gyrokinetic mode. In addition to KBMs and TEMs, we consider micro-tearing modes (MTMs) [82–85], electron-temperature-gradient (ETG) modes [30, 64, 86, 87], tearing ETG (TETG) modes [88], and ion-temperature-gradient (ITG) modes [29, 45, 89, 90]. In Table 1, χ_s and D_s are the turbulent heat and particle diffusivities (later defined in Equation (9)), $\mathcal{P}(A_\parallel) = 1 - |\int A_\parallel d\theta|/\int |A_\parallel| d\theta$ [91] is the mode parity in the fluctuating field $A_\parallel$, γ is the linear growth rate, and ω_R is the real frequency.

Because of the wide range of devices we study and the often unusual nature of gyrokinetic instabilities in the pedestal, many of the mode criteria quantities in Table 1 are not hard cutoffs, but rather, approximate values that the mode should satisfy – the more criteria that a given instability satisfies, the more confidence in a given mode type identification. In our experience, distinguishing between KBM, TEM, and ITG was often challenging and required using $D_e/(\chi_e+\chi_i)$ and $\partial\gamma/\partial\beta$. With the exception of the MTM, we ignore the mode's real frequency in automated mode identification. For all gyrokinetic and ideal simulations in this paper, we only study the radial wavenumber $k_x = 0$ because we focus on KBM stability. While $k_x = 0$ is typically the most unstable mode for KBM [92], for other instabilities this may not be the case [86, 93–97].

We also perform ideal infinite-n ballooning simulations at the same radial locations as the gyrokinetic simulations. At each flux-surface, there are three stability states for the ideal mode: first-stable, unstable, and second-stable.

2.3 The Ballooning and Gyrokinetic Critical Pedestal

In this section, we describe the calculation of the Gyrokinetic Critical Pedestal (GCP) and Ballooning Critical Pedestal (BCP) [8] using information from gyrokinetic and ideal infinite-n simulations.

Extensive experimental and theoretical work has shown that the pedestal pressure gradient is often limited by ballooning modes [8, 26, 98–100]. In this work, we focus on ballooning instabilities that limit the pressure gradient in the steep-gradient regions of the pedestal, although there are examples of pedestal

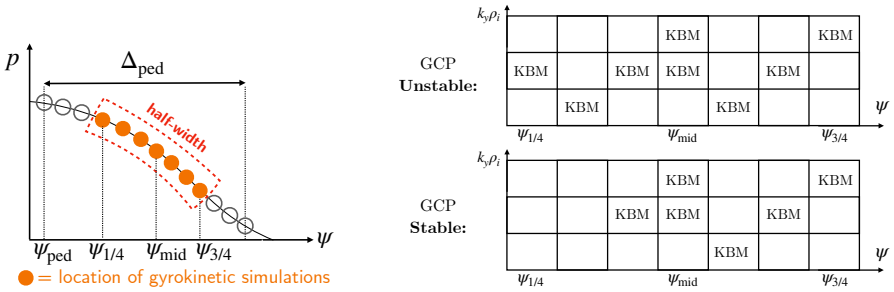

(a) Locations of gyrokinetic simulations in pedestal half-width

(b) GCP calculation with dominant gyrokinetic instability versus binormal wavenumber $k_y\rho_i$ and radial location ψ.

Figure 2: Schematics of (a) gyrokinetic simulation radial locations and (b) Gyrokinetic Critical Pedestal (GCP) calculation with dominant gyrokinetic instability versus binormal wavenumber $k_y\rho_i$ and radial location ψ. Top: GCP unstable example since KBM unstable for at least a single $k_y\rho_i$ value at each radial location. Bottom: GCP stable location. Only KBM stability status is shown.

regimes where ballooning instabilities at the pedestal foot, not the steep-gradient region, are limiting [101]. In the EPED model, the ideal infinite-n mode is hypothesized to set the steepest pressure gradient a pedestal achieves across the pedestal half-width. If every radial location within the half-width is ideal-ballooning unstable, EPED determines that the pedestal profile is no longer physically accessible, a constraint known as the Ballooning Critical Pedestal (BCP) [8]. The EPED model has been applied successfully to multiple experiments [5, 9–12]. However, recent work [28] showed that for ELMy NSTX pedestals, kinetic-ballooning – rather than ideal-ballooning – stability is needed to match width-height scalings with experiment [13]. Such a constraint using the KBM stability threshold is called the Gyrokinetic Critical Pedestal (GCP) [28, 102, 103]. The pedestal half-width region used for the BCP and GCP is shown schematically in Figure 2(a). For the GCP calculation, if KBM is unstable at any $k_y\rho_i$ wavenumber for a given radius, that radius counts as 'unstable' toward the GCP calculation. If all radii within the pedestal half-width are 'unstable,' the pedestal is GCP unstable. A GCP unstable and stable pedestal are shown schematically in Figure 2(b).

Practically, to find the BCP and GCP we start from an input equilibrium, typically calculated from an experiment, and construct a set of equilibria with varied pedestal width and height as outlined in Section 2.1. We then evaluate ideal-ballooning and gyrokinetic stability across the pedestal half-width on all of these equilibria, and find the boundary in $\Delta_{\rm ped}$, $\beta_{\theta,\rm ped}$ coordinates between equilibria that are accessible and inaccessible according to the BCP and GCP. A width-height scaling is found by fitting this boundary to a function with constants C and G

$$\Delta_{\rm ped} = C\,(\beta_{\theta,\rm ped})^{G}\,. \tag{6}$$

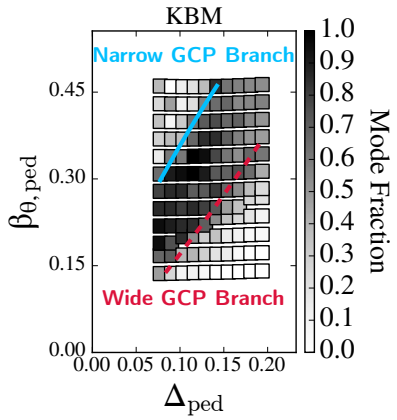

Figure 3: Fraction of KBM dominance across the pedestal half-width for fixed $n_{e,\mathrm{ped}}$ in NSTX 139047, with wide and narrow GCP branches. The mode fraction is the fraction of all linear gyrokinetic simulations across the pedestal half-width and binormal wavenumbers (here $k_y\rho_i \in [0.06, 0.12, 0.18]$) where the fastest growing mode is classified as KBM, MTM, etc.

In this paper we describe the two cases of varying $\beta_{\theta,\mathrm{ped}}$ at fixed $n_{e,\mathrm{ped}}$ and fixed $T_{e,\mathrm{ped}}$, which previous work [28] has shown gave significant differences in the width-height scaling.

2.4 Pedestal Bifurcation

Recently, it was shown that a bifurcation in KBM stability caused by aspect-ratio and shaping might be responsible for the variation in width-height scaling across devices [102]. If both first and second KBM stability can be accessed robustly across the pedestal half-width at different widths and heights, this led to two solutions for Δ_{ped}: a wide and narrow GCP branch. In Figure 3, we show an example of an equilibrium where both the wide and narrow GCP branches exist. The mode fraction in Figure 3 corresponds to the fraction of all modes across the pedestal half-width and simulated $k_y\rho_i$ wavenumbers that are KBMs. In Figure 3, three binormal wavenumbers are used $k_y\rho_i \in [0.06, 0.12, 0.18]$, so the minimum KBM mode fraction required to trigger the wide or narrow GCP is 1/3. Throughout this paper, we will refer frequently to the wide and narrow GCP branches.

It has also been demonstrated that there is a bifurcation in the macroscopic constraint for pedestal prediction, peeling-ballooning-mode (PBM) stability. It was predicted [11] and then demonstrated experimentally in DIII-D and C-Mod [5] that a second PBM-stable region at higher pressure exists for sufficiently strong triangularity and high density. In TCV, it was also predicted that by varying the triangularity from negative to positive decreased the pedestal height by a factor of 4 [26] due to differences in PBM stability.

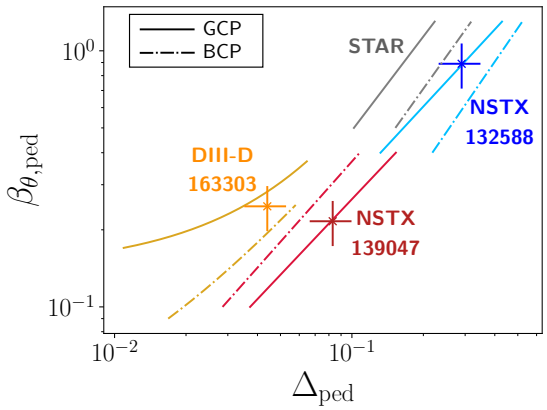

Figure 4: Gyrokinetic Critical Pedestal (GCP) and Ballooning Critical Pedestal (BCP) scaling expressions with experimental points indicated by markers and uncertainty bars of 20 %. The design point for STAR has not yet been finalized.

3 Device Scan

In this section, we give examples of the GCP and BCP calculations for NSTX, DIII-D, and STAR devices. The GCP for more devices is given in [102].

3.1 NSTX

We study two NSTX discharges: NSTX 139047 is an ELMy NSTX H-mode [13], and NSTX 132588 [104] is a ultra-wide-pedestal lithiated enhanced-pedestal (EP) H-mode. In Figure 4 we plot the GCP with solid lines and the BCP with dash-dotted lines. For both NSTX 139047 and NSTX 132588, the width-height scaling expression is in excellent agreement with the experimental point, strong evidence that KBM is limiting the pedestal width and height. Notably, for NSTX 139047, the GCP gives a less steep pedestal than the BCP, indicating that the pedestal is limited by KBM first-stability, and therefore is the wide GCP. In contrast, for NSTX 132588, the GCP gives a steeper pedestal than the BCP, indicating that the pedestal is in KBM second-stability and is therefore the narrow GCP. Plotted in Figure 4, the NSTX 132588 GCP scaling is $\Delta_{\mathrm{ped}} = 0.33\beta_{\theta,\mathrm{ped}}^{1.03}$ and the NSTX 139047 GCP scaling is $\Delta_{\mathrm{ped}} = 0.39\beta_{\theta,\mathrm{ped}}^{1.02}$ [28].

3.2 DIII-D

We now find the BCP and GCP for DIII-D 163303 [105], a previously published ELMy H-mode discharge that is used to study wall conditions, the L-H transition power threshold, and outgassing. Shown in Figure 4, the experimental point for this equilibrium is at a $\beta_{\theta,\mathrm{ped}}$ value slightly above the ballooning critical pedestal but slightly below the gyrokinetic critical pedestal. However, within 20% uncertainty, this equilibrium is consistent with both the BCP and GCP,

indicating that this pedestal is likely ballooning-limited. Plotted in Figure 4, the DIII-D 163303 GCP scaling is is $\Delta_{\rm ped} = 0.31\beta_{\theta,\rm ped}^{0.37} - 0.15$.

3.3 STAR

The Spherical Tokamak Advanced Reactor (STAR) is an $A = 2$, $R_0 = 4$m compact high-field tokamak [106] targeting 100-500 MWe net electric power. Here, $A = R_0/a$ is the aspect-ratio for minor radius and major radius R_0. In Figure 4, the STAR device is shown to achieve high values of $\beta_{\theta,\rm ped}$ while having a narrower pedestal. Similar to NSTX discharge 132588, STAR relies on accessing KBM second-stability to obtain its steeper kinetic-ballooning-constrained pedestals, which shown in Figure 4, causes the GCP to give a steeper pedestal prediction than the BCP. A final $\beta_{\theta,\rm ped}$, $\Delta_{\rm ped}$ design point has not yet been determined. Notably, STAR achieves a relatively steeper pedestal measured approximately by $\beta_{\theta,\rm ped}/\Delta_{\rm ped}$ due to its low magnetic shear values across most of the pedestal, causing the KBM and ideal-ballooning-mode to be second stable. Plotted in Figure 4, the STAR GCP scaling is $\Delta_{\rm ped} = 0.18\beta_{\theta,\rm ped}^{0.82}$.

4 Aspect-Ratio and Shaping Scan

In this section, we describe briefly aspect-ratio and shaping scans on ELMy NSTX discharge 132543 [107]. We choose a Luce parameterization for the last-closed-flux-surface shape [108]. We define the flux surface elongation κ and triangularity δ as the average $\langle \ldots \rangle_L$ of the Luce parameters $\kappa = \langle \kappa \rangle_L$, $\delta = \langle \delta \rangle_L$. The gk_ped tools can perform aspect-ratio and shaping scans and find the BCP and GCP scaling expressions from the resulting new equilibria. The shaping and aspect-ratio scaling results for a different NSTX equilibrium are detailed in [102].

For aspect-ratio scans, we use EFIT-AI [62] to construct new equilibria for a range of aspect-ratios keeping the minor radius a constant but allowing the major radius R_0 to vary. In Figure 5(a), we plot the last-closed-flux-surfaces for $A \in [1.5, 1.96, 2.42, 2.88, 3.34, 3.8]$ – for each aspect-ratio, a new magnetic coilset is generated by modifying the aspect-ratio of a basecase NSTX coilset, which is used to generate the Green's functions needed for free-boundary equilibrium reconstruction by the EFUND code [63]. The boundary points are fixed and the equilibrium parameters are rescaled as follows $\beta_N \sim 1/\sqrt{R_0}$, $B_T \sim R_0$, $I_p \sim \sqrt{R_0}$. This gives $q_{95} \sim R_0^{-3}$ and bootstrap fraction, $f_{\rm bs} \sim R_0^{-0.9}$. In Figure 5(b), we show how these quantities vary with aspect-ratio. For the highest major radius $R_0 \simeq 2.4$m, the flux-function $R_0 B_{T0} \simeq 2.4$[Tm], which is comparable to or lower than JET [109], SPARC [6], and DIII-D [110]. Thus, our high-aspect-ratio equilibria respect reasonable engineering requirements for $R_0 B_{T0}$.

For triangularity scans, we fit the last-closed-flux-surface using a Luce parameterization and rescale $\delta = (\delta_{\rm upper} + \delta_{\rm lower})/2$ by a scalar factor. When varying triangularity, we keep all other plasma parameters constant. For elongation scans, we choose to vary the plasma current in order to keep β_N constant.

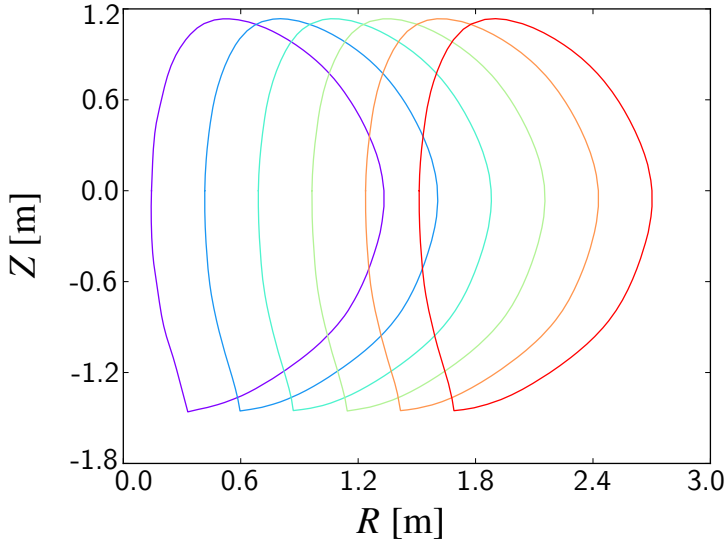

(a) Last-closed-flux-surfaces across aspect-ratio.

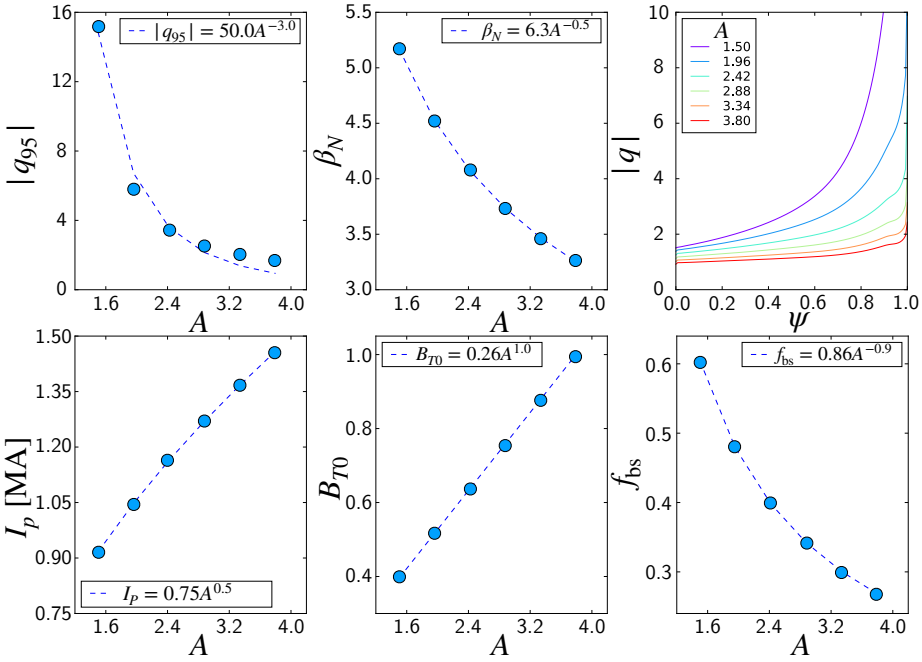

(b) Top row, left to right: q_{95}, β_N, q. Bottom row: I_p, B_{T0}, f_{BS}.

Figure 5: Equilibrium quantities for aspect-ratio scan in NSTX 132543.

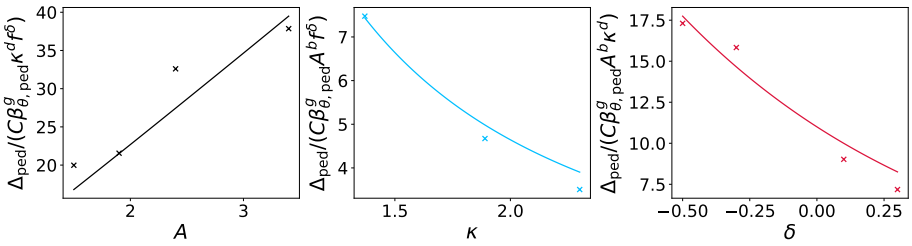

Figure 6: Fitting of $\Delta_{\rm ped}$ in Equation (7) to 11 shaping variations of NSTX discharge 132543, where the dependence on A, κ, and δ is shown in each subplot. For simplicity, we only show points where the x-axis parameter has changed from the nominal value.

Given $\beta_T \sim (1+\kappa^2)\beta_N^2$, in order to keep β_N constant we vary plasma current as $I_p \sim 1+\kappa^2$ at fixed A, a, B_T [111].

Once the equilibria with different aspect-ratio and shaping are generated, we evaluate the Gyrokinetic Critical Pedestal for each equilibrium.

4.1 Least-Squares Fit

Based on our shaping and aspect-ratio scans, we perform a least-squares fit for the pedestal width of the form

$$\Delta_{\rm ped} = CA^b\kappa^d f^\delta \left(\beta_{\theta,\rm ped}\right)^g , \tag{7}$$

using the GCP from 11 shaping scans for NSTX 132543. In this paper, we fit the GCP width-scaling for only the wide GCP branch, finding

$$\Delta_{\rm ped} = 0.92A^{1.04}\kappa^{-1.24}0.38^\delta\beta_{\theta,\rm ped}^{1.05}, \tag{8}$$

with functional dependencies similar to fits performed in [102] for a different NSTX equilibrium. The fitting parameters in Equation (8) have the values and standard deviation uncertainty: $C = 0.92 \pm 0.16$, $b = 1.04 \pm 0.16$, $d = -1.24 \pm 0.26$, $f = 0.38 \pm 0.04$, $g = 1.05 \pm 0.12$. In Figure 6, we plot the normalized width versus fitting and shaping parameters A, κ, and δ. The R^2 value for all fitting parameters is $R^2 = 0.94$, indicating a relatively good fit. Removing any one of A, κ, δ reduced the R^2 value significantly, indicating the importance of all three of these parameters. This analysis can be improved in future work by: (1) increasing sample size, (2) performing fits on multi-discharge and multi-device experimental database, (3) a comprehensive assessment of more shaping and plasma parameters to find the most important parameters determining $\Delta_{\rm ped}$. The narrow branch width-height-shaping scaling expressions can be found in [102].

Table 2: Aspect-ratio scan parameter values for NSTX 139047 used in Section 5.

Name	$A = R_0/a$	B_T [T]	I_p [MA]
A_1	1.6	0.45	0.93
A_2	2.0	0.55	1.0
A_3	2.5	0.68	1.1
A_4	2.9	0.81	1.2

5 Turbulent Transport Near The Gyrokinetic Critical Pedestal

In this section, we relate the pedestal width scaling to turbulent transport. We also use transport ratios from linear gyrokinetic simulations to study turbulent transport in the vicinity the GCP first and second stable branches. In these regions, the heat to particle transport ratios from KBM stability can vary significantly compared with transport in strongly-driven KBM regions. Given that experimentally the pedestal is often close to the GCP and far from the strongly-driven KBM regions, the changing transport properties of KBM and other modes has implications for the evolution of density and temperature profiles. In this section, we use equilibria based on NSTX discharge 139047 that have a range of aspect-ratio values, detailed in Table 2. Unless mentioned otherwise, the nominal case used is NSTX discharge 139047 with a slightly increased aspect-ratio $A = 2.0$, referred to as A_2.

5.1 Gyrokinetic Stability and Transport

Linear gyrokinetic simulations provide information about dominant mode type around the GCP. In Figure 7, we plot the fraction of different mode types across the pedestal half-width for binormal wavenumbers $k_y\rho_i \in [0.06, 0.12, 0.18]$ for NSTX discharge 139047 A_2. In the GCP unstable region, KBM dominates, with mode fractions lying in $0.5 - 1.0$. At pressures below the wide GCP branch, MTM is ubiquitous and for pressures above the narrow GCP branch, TEM is the most common mode. We expect TEM instability generally for higher $k_y\rho_i$ values than included in these simulations, which explains the relatively low TEM fraction at pressures above the narrow GCP in Figure 7(d).

In addition to mode type, linear gyrokinetic simulations give flux and diffusivity ratios. The gyroBohm-normalized heat and particle fluxes through a flux surface are

$$\begin{aligned} q_s &= \langle \int \frac{m_s v^2}{2} h_s \mathbf{v}_\chi \cdot \frac{\nabla\psi}{|\nabla\psi|} d^3v \rangle_\psi / q_{\mathrm{gB}} = \chi_s \frac{a}{L_{T_s}} + \frac{3}{2}\Gamma_s, \\ \Gamma_s &= \langle \int h_s \mathbf{v}_\chi \cdot \frac{\nabla\psi}{|\nabla\psi|} d^3v \rangle_\psi / \Gamma_{\mathrm{gB}} = D_s \frac{a}{L_{n_s}}, \end{aligned} \tag{9}$$

where $\langle \ldots \rangle_\psi$ is a flux-surface average, m_s is the particle mass, q_s and Γ_s are the gyroBohm normalized heat and particle fluxes for a species s, χ_s and D_s are the

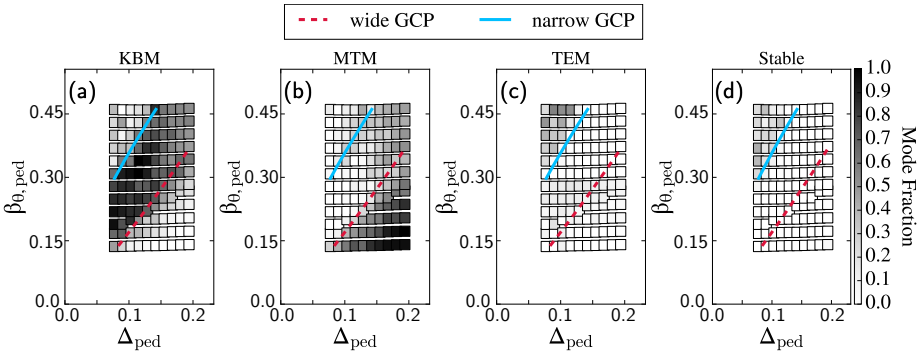

Figure 7: Fraction of gyrokinetic mode types across the pedestal half-width for fixed $n_{e,\mathrm{ped}}$ in NSTX 139047 A_2. The mode fraction is the fraction of all linear gyrokinetic simulations across the pedestal half-width and binormal wavenumbers (here $k_y\rho_i \in [0.06, 0.12, 0.18]$) where the fastest growing mode is classified as KBM, MTM, etc.

normalized heat and particle diffusivities, and $q_{\mathrm{gB}} = \rho_{*r}^2 n_r T_r \bar{c}$, $\Gamma_{gB} = \rho_{*r}^2 n_r \bar{c}$ where r subscripts refer to a reference species, $\bar{c} = \sqrt{T_e/m_D}$ is the sound speed, and $\rho_{*r} = \rho_r/a$ where ρ_r is the gyroradius. The ratio of heat to particle flux is

$$\frac{q_s}{\Gamma_s} = \eta_s \frac{\chi_s}{D_s} + \frac{3}{2}, \tag{10}$$

where $\eta_s = \nabla \ln T_s / \nabla \ln n_s$. Thus, changing η_s by varying pedestal height via density or temperature can affect strongly the heat and particle flux ratios, even if χ_s/D_s is constant.

We find the ratio χ_e/D_e varies significantly around the GCP. In the top row of Figure 8, we plot χ_e/D_e versus $\beta_{\theta,\mathrm{ped}}$ and Δ_{ped} for KBM, MTM, and TEM instability in NSTX discharge 139047 A_2. In strongly driven KBM regions of Figure 8(a), $\chi_e/D_e \simeq 1.5$. However, as the KBM is stabilized near the narrow and wide GCP branches, its transport coefficients change, often satisfying $\chi_e/D_e \simeq 2-5$. For MTM instability in Figure 8(b), $\chi_e/D_e \simeq 10-50$, and for TEM in Figure 8(c), $-1 \lesssim \chi_e/D_e \lesssim 2$. Negative values of $(\chi_i + \chi_e)/D_e$ have been reported and explained by a particle pinch [56], which could explain why we find $\chi_e/D_e < 0$ for TEM. While nonlinear simulations [112] are required for accurate flux ratios, the strong variation of χ_e/D_e close to marginal stability presents challenges to reduced transport-based pedestal models [19, 113].

Around the GCP, χ_e/D_C is much larger than reported in the literature [56] where it was reported $\chi_e/D_C \simeq 3/2$. Here, D_C is the Carbon-12 particle diffusivity. Plotted in Figure 8(d), along the wide GCP $\chi_e/D_C \simeq 15-20$, indicating that KBM produces relatively weak impurity transport in the inter-ELM period. We use the ratio $(\chi_e + \chi_D)/D_e$ [56] to distinguish between KBM and TEM, where χ_D is the heat diffusivity for the main ion deuterium. For KBM along the GCP we find $(\chi_e + \chi_D)/D_e \simeq 3$, increasing substantially near marginal KBM stability to $(\chi_e + \chi_D)/D_e \simeq 10$.

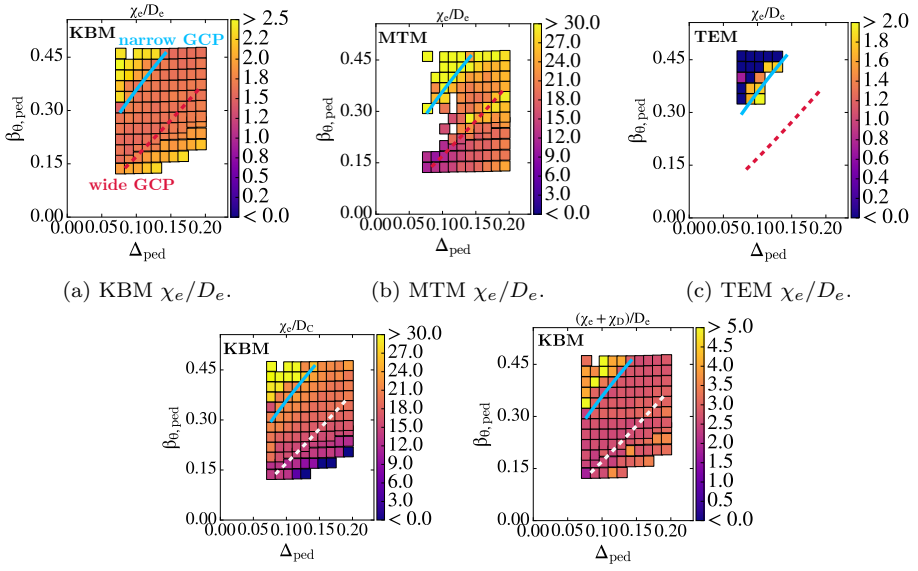

(a) KBM χ_e/D_e. (b) MTM χ_e/D_e. (c) TEM χ_e/D_e.

(d) KBM χ_e/D_C. (e) KBM $(\chi_e+\chi_D)/D_e$.

Figure 8: Top row: electron diffusivities D_e/χ_e for KBM, MTM, and TEM for NSTX 139047 A_2. Bottom row: KBM χ_e/D_C and $(\chi_e+\chi_D)/D_e$.

The transport coefficients in different GCP regions are summarized later in Table 3 and are discussed more in Section 5.3.

5.2 Width-Transport Scaling

In this section, we take initial steps in relating pedestal width and transport. While linear stability threshold models [8, 28] provide width-height scalings, they omit the sources and transport required to sustain pedestal profiles. Here, we find the dependence of pedestal width on the transport ratio q_e/Γ_e. To simplify analysis, we study quantities averaged over the pedestal half-width,

$$\left\langle \frac{q_e}{\Gamma_e} \right\rangle_{\mathrm{ped}} = \int_{\psi_{1/4}}^{\psi_{3/4}} \frac{q_e}{\Gamma_e}\, d\psi \Big/ \int_{\psi_{1/4}}^{\psi_{3/4}} d\psi = (2/\Delta_{\mathrm{ped}}) \int_{\psi_{1/4}}^{\psi_{3/4}} \frac{q_e}{\Gamma_e}\, d\psi, \tag{11}$$

where $\psi_{1/4} = \psi_{\mathrm{mid}} - \Delta_{\mathrm{ped}}/4$ and $\psi_{3/4} = \psi_{\mathrm{mid}} + \Delta_{\mathrm{ped}}/4$. Along the GCP, if KBM dominates electron heat and particle transport and $\chi_{e,\mathrm{KBM}}/D_{e,\mathrm{KBM}} = 3/2$ is constant, radially averaging Equation (10) gives

$$\left\langle \frac{q_s}{\Gamma_s} \right\rangle_{\mathrm{ped},3/2} = \frac{3}{2}\left(\langle \eta_e \rangle_{\mathrm{ped}} + 1\right), \tag{12}$$

where the 3/2 subscript in $\langle q_e/\Gamma_e \rangle_{\mathrm{ped},3/2}$ indicates that we assumed $\chi_e/D_e = 3/2$. In Figure 9(a), we plot $\langle q_e/\Gamma_e \rangle_{\mathrm{ped},3/2}$ along the GCP wide branch using

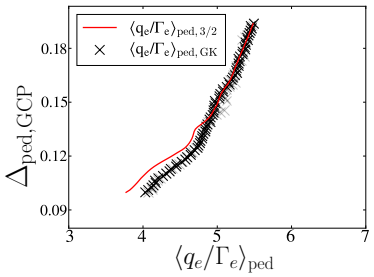

(a) Width versus $\langle q_e/\Gamma_e\rangle_{\rm ped}$ along wide GCP branch at fixed $n_{e,\rm ped}$ for transport model $\langle q_e/\Gamma_e\rangle_{\rm ped,3/2}$ and simulations $\langle q_e/\Gamma_e\rangle_{\rm ped,GK}$.

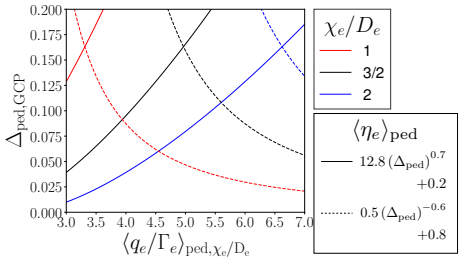

(b) Width prediction using two different fits of $\langle \eta_e\rangle_{\rm ped}$ for three $\chi_e/D_e \in [1, 1.5, 2.0]$ values for the KBM.

Figure 9: Pedestal width along the GCP versus $\langle q_e/\Gamma_e\rangle_{\rm ped}$ from gyrokinetic simulations and a transport model in Equation (15) for NSTX 139047 A_2. In (a), we use the exact values of $\langle \eta_e\rangle_{\rm ped}$ to calculate $\langle q_e/\Gamma_e\rangle_{\rm ped,3/2}$. In (b), a best fit is used for $\langle q_e/\Gamma_e\rangle_{\rm ped,\chi_e/D_e}$.

Equation (12) for NSTX 139047 A_2 and also plot $\langle q_e/\Gamma_e\rangle_{\rm ped,GK}$ using data from KBMs in gyrokinetic simulations,

$$\left\langle \frac{q_s}{\Gamma_s}\right\rangle_{\rm ped,GK} = \frac{\sum_{k_y}\int_{\psi_{1/4}}^{\psi_{3/4}} q_e/\Gamma_{e\rm KBM}(\psi,k_y)\,d\psi}{\sum_{k_y}\int_{\psi_{1/4}}^{\psi_{3/4}} d\psi}, \tag{13}$$

where $\sum_{k_y}$ is a sum over all k_y wavenumbers included in the simulation and $q_e/\Gamma_{e\rm KBM}$ is evaluated only if the fastest growing mode is a KBM. The close agreement between $\langle q_e/\Gamma_e\rangle_{\rm ped,3/2}$ and $\langle q_e/\Gamma_e\rangle_{\rm ped,GK}$ in Figure 9(a) demonstrates that $\chi_e/D_e = 3/2$ is an excellent approximation for the KBM along this particular wide branch GCP.

We now obtain an expression for $\Delta_{\rm ped,GCP}$ as a function of $\langle q_e/\Gamma_e\rangle_{\rm ped,3/2}$ by relating $\langle \eta_e\rangle_{\rm ped}$ to $\Delta_{\rm ped,GCP}$ through $\beta_{\theta,\rm ped,GCP}$. It is useful to obtain $\Delta_{\rm ped,GCP}$ through η_e because later we will examine how varying $\beta_{\theta,\rm ped}$ with constant $n_{\rm ped}$ or constant $T_{\rm ped}$ affects η_e and therefore pedestal width. We write the dependence of $\langle \eta_e\rangle_{\rm ped}$ on $\beta_{\theta,\rm ped,GCP}$,

$$\langle \eta_e\rangle_{\rm ped} = a_1\left(\beta_{\theta,\rm ped,GCP}\right)^{\alpha_1} + d = a_1 D^{\alpha_1}\left(\Delta_{\rm ped,GCP}\right)^{\alpha_1\alpha_2} + d, \tag{14}$$

where we used the GCP relation $\beta_{\theta,\rm ped,GCP} = D\left(\Delta_{\rm ped,GCP}\right)^{\alpha_2}$. Substituting Equation (14) into Equation (12) gives $\Delta_{\rm ped,GCP}$ as a function of $\langle q_e/\Gamma_e\rangle_{\rm ped,3/2}$,

$$\Delta_{\rm ped,GCP} = \left(\frac{\frac{2}{3}\langle \frac{q_e}{\Gamma_e}\rangle_{\rm ped,3/2} - (1+d)}{a_1\,(D)^{\alpha_1}}\right)^{1/(\alpha_1\alpha_2)}. \tag{15}$$

For fixed $n_{\rm ped}$, we find $\alpha_1 = 0.55$, $\alpha_2 = 1.2$, $d = 0.165$, $a_1 = 4.33$, and $D = 2.47$,

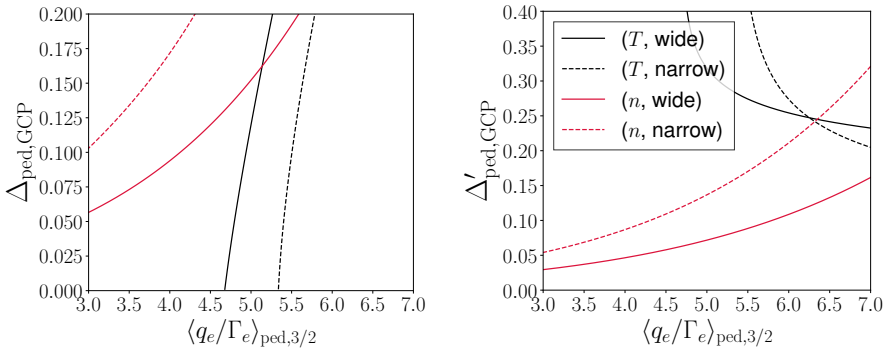

(a) Δ_{ped} versus $\langle q_e/\Gamma_e\rangle_{\mathrm{ped},3/2}$. (b) Δ'_{ped} versus $\langle q_e/\Gamma_e\rangle_{\mathrm{ped},3/2}$.

Figure 10: Pedestal width (Equation (15)) and its derivative $\Delta'_{\mathrm{ped}} = d\Delta_{\mathrm{ped}}/d\langle q_e/\Gamma_e\rangle_{\mathrm{ped},3/2}$ as a function of $\langle q_e/\Gamma_e\rangle_{\mathrm{ped},3/2}$ for NSTX 139047 A_2. We show four GCP branches: wide and narrow for fixed $n_{e,\mathrm{ped}}$ (red) and fixed $T_{e,\mathrm{ped}}$ (black).

giving a wide GCP width-transport scaling

$$\Delta_{\mathrm{ped,wide\ GCP,fixed\ n}} \simeq 0.028\left(\left\langle\frac{q_e}{\Gamma_e}\right\rangle_{\mathrm{ped},3/2} - 1.7\right)^{1.5}. \tag{16}$$

In Figure 9(b), in solid lines we plot $\Delta_{\mathrm{ped,GCP}}$ in Equation (15) for three values of $\chi_{e,\mathrm{KBM}}/D_{e,\mathrm{KBM}} \in [1, 3/2, 2]$ using the fitted form of $\langle\eta_e\rangle_{\mathrm{ped}}$ in Equation (14): The pedestal width is very sensitive to the $\chi_{e,\mathrm{KBM}}/D_{e,\mathrm{KBM}}$ value used in $\langle q_e/\Gamma_e\rangle_{\mathrm{ped}}$. Using $\chi_e/D_e = 2$ we find $\Delta_{\mathrm{ped,GCP}} \simeq 0.025$ at $\langle q_e/\Gamma_e\rangle_{\mathrm{ped}} = 3.5$, but using $\chi_e/D_e = 1$ we find $\Delta_{\mathrm{ped,GCP}} \simeq 0.2$. Therefore, a 2x decrease in χ_e/D_e gives an 8x increase in $\Delta_{\mathrm{ped,GCP}}$.

In Figure 9(b), using dashed lines we also plot $\Delta_{\mathrm{ped,GCP}}$ for an $\langle\eta_e\rangle_{\mathrm{ped}}$ function that depends *inversely* with $\Delta_{\mathrm{ped,GCP}}$: $\langle\eta_e\rangle_{\mathrm{ped}} = 0.5\,(\Delta_{\mathrm{ped}})^{-0.6} + 0.8$, but using the same width-height scaling relation. Such an inverse relation for Δ_{ped} and $\langle\eta_e\rangle_{\mathrm{ped}}$ would result from varying $\beta_{\theta,\mathrm{ped}}$ at fixed $T_{e,\mathrm{ped}}$ and fixed $n_{e,\mathrm{sep}}$ (see Equation (29), Appendix A). The widest pedestals are given by the largest $\chi_{e,\mathrm{KBM}}/D_{e,\mathrm{KBM}}$ values rather than the smallest $\chi_{e,\mathrm{KBM}}/D_{e,\mathrm{KBM}}$, which happened when $\langle\eta_e\rangle_{\mathrm{ped}}$ increased with $\Delta_{\mathrm{ped,GCP}}$.

By varying pedestal height at fixed $T_{e,\mathrm{ped}}$ for NSTX discharge 139047 A_2, $\Delta_{\mathrm{ped,GCP}}$ is much more sensitive to $\langle\eta_e\rangle_{\mathrm{ped}}$, making $\Delta_{\mathrm{ped,GCP}}$ more sensitive to $\langle q_e/\Gamma_e\rangle_{\mathrm{ped}}$ at fixed $T_{e,\mathrm{ped}}$ than at fixed $n_{e,\mathrm{ped}}$. At fixed $T_{e,\mathrm{ped}}$, we find the width-transport scaling,

$$\Delta_{\mathrm{ped,wide\ GCP,fixed\ T}} \simeq 0.31\left(\left\langle\frac{q_e}{\Gamma_e}\right\rangle_{\mathrm{ped},3/2} - 4.7\right)^{0.85}. \tag{17}$$

The stronger sensitivity of pedestal width to $\langle q_e/\Gamma_e\rangle_{\mathrm{ped}}$ at fixed $T_{e,\mathrm{ped}}$ occurs because we keep $n_{\mathrm{ped}}/n_{\mathrm{sep}}$ fixed when increasing β_{ped}, making η_e only weakly

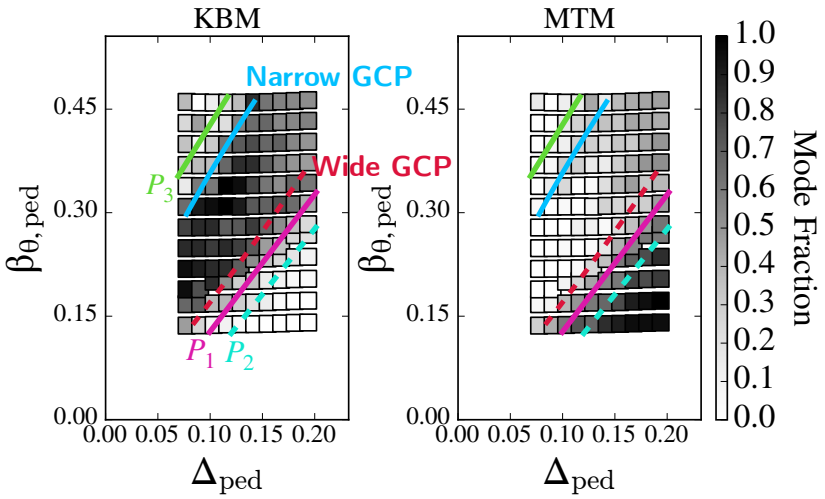

Figure 11: Paths P_1, P_2, and P_3 in the vicinity of the wide and narrow GCPs, plotted over KBM and MTM mode dominance fraction versus pedestal width and height for NSTX 139047 A_2. The mode fraction is the fraction of all linear gyrokinetic simulations across the pedestal half-width and binormal wavenumbers (here $k_y\rho_i \in [0.06, 0.12, 0.18]$) where the fastest growing mode is classified as KBM, MTM, etc.

dependent on β_{ped}. In Figure 10(a) we plot $\Delta_{\mathrm{ped,GCP}}$ for fixed $n_{e,\mathrm{ped}}$ and fixed $T_{e,\mathrm{ped}}$ narrow and wide GCP branches using the fitted form of $\Delta_{\mathrm{ped,GCP}}$ in Equation (15) – notably, the black curves corresponding to fixed $T_{e,\mathrm{ped}}$ narrow and wide GCP branches have relatively large derivatives, as shown in Figure 10(b). This suggests that for KBM-limited pedestals with fixed $T_{e,\mathrm{ped}}$, a small increase of $\langle q_e/\Gamma_e\rangle_{\mathrm{ped},3/2}$ (e.g. decreased fueling) would increase Δ_{ped} much more effectively than increasing $\langle q_e/\Gamma_e\rangle_{\mathrm{ped}}$ by increasing the heating.

To summarize, Equations (16) and (17) are the wide GCP pedestal width-transport expressions resulting from a simple transport model that assumes along the GCP, turbulent particle *and* heat transport are dominated by the KBM with a transport ratio $\chi_e/D_e = 3/2$. Equations (16) and (17) have noteworthy features: (a) there is a minimum level of transport $\langle q_e/\Gamma_e\rangle_{\mathrm{ped},3/2} \simeq 3(1+d)/2$ required for $\Delta_{\mathrm{ped}} > 0$, (b) if $\langle \eta_e\rangle_{\mathrm{ped}}$ is independent of $\beta_{\theta,\mathrm{ped}}$, then a fixed $\langle q_e/\Gamma_e\rangle_{\mathrm{ped}}$ value can support any pedestal width, and (c) Δ'_{ped} is an increasing function of $\langle q_e/\Gamma_e\rangle_{\mathrm{ped},3/2}$ at fixed $n_{e,\mathrm{ped}}$ but decreasing for fixed $T_{e,\mathrm{ped}}$.

In the next section, we show that in marginally stable regions close to – but not exactly along – the GCP, transport ratios can differ substantially.

5.3 Transport Around GCP Marginality

In this section, we describe turbulent transport ratios in the vicinity of the wide and narrow GCP branches for NSTX 139047 A_2. The wide and narrow GCP branches can be seen as experimental bounds for $\beta_{\theta,\mathrm{ped}}$: KBM-limited pedestals

Table 3: KBM transport coefficients in NSTX 139047 A_2 in different GCP regions.

GCP	χ_e/D_e	χ_e/D_C
Strongly Unstable	$\simeq 3/2$	$\simeq 15-25$
Stable, Near Wide Branch	$\simeq 3/2-5/2$	$\simeq 25-40$
Stable, Near Narrow Branch	$\simeq 3/2-5$	$\simeq 5-15$

may not fall exactly on the GCP branches in the inter-ELM cycle. Therefore, it is instructive to study transport not just along the GCP, but also in its vicinity.

Transport ratios change at pressures below the wide GCP scaling. Consider a path where rather than all radial locations in the pedestal half-width being unstable to KBM, only half of all radial locations are unstable – this is shown by path P_1 in Figure 11. Along P_1 there is still a substantial KBM mode fraction (roughly 1/3 of modes), so KBM transport may still be expected. Of the remaining KBMs, χ_e/D_e and χ_e/D_C both increase, meaning that electron and impurity particle transport are increasing relative to heat transport. In Table 3, we summarize the KBM transport properties of P_1 in the 'Stable, Near Wide Branch' row. Along a trajectory above the narrow BCP branch, path P_3 in Figure 11, the ratio χ_e/D_e also increases while χ_e/D_C decreases. This indicates that KBM impurity particle transport might be more significant in the narrow than the wide branch.

Non-KBM transport is likely increasingly important further away from the GCP. Consider the path P_2 in Figure 11 where the pedestal is at a pressure far below the GCP. Here, the KBM is close to marginally stable at all pedestal flux surfaces. Shown in Figure 11(b), the MTM has a significant mode fraction along P_2 for the $k_y\rho_i$ values we simulate, indicating significant electron heat transport. Given that KBM is subdominant along P_2, another mechanism such as TEM or neoclassical physics is required for particle transport.

5.4 Aspect-Ratio Dependence

In this section, we show how transport near the GCP varies across aspect-ratio.

Along the wide GCP, χ_e/D_e along the wide GCP branch is larger at is higher-A ($\chi_e/D_e \simeq 2-2.5$) than at lower-A ($\chi_e/D_e \simeq 1.5$). At lower-A, any remaining KBM instabilities also have a higher growth rate than at higher-A along the wide GCP branch, shown in Figure 12 where we plot the average growth rate γ of KBM modes for NSTX 139047 A_2 (A = 2.0) and A_4 (A = 2.9). Here, γ is normalized by the minor radius a and sound speed $\bar{c}$. This indicates that the more unstable KBMs along the lower-A wide GCP branch have transport properties expected for an MHD mode $\chi_e/D_e = 3/2$. At lower growth rates close to KBM marginality, the higher-A KBM has modified transport properties where kinetic effects appear to be particularly important. However, along the narrow GCP branch for both lower and higher aspect-ratio in Figure 12, the KBM growth rate decreases sharply around the narrow GCP boundary, indicating that KBM transport changes quickly across the boundary.

The differing KBM transport coefficients across aspect-ratio along the GCP

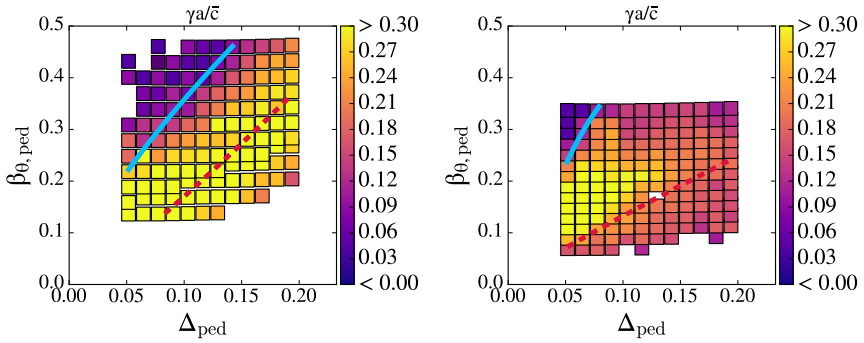

(a) Aspect-ratio = 2.0 (b) Aspect-ratio = 2.9

Figure 12: KBM linear growth rates averaged over the pedestal half-width and all simulated wavenumbers versus Δ_{ped} and $\beta_{\theta,\mathrm{ped}}$ for two aspect-ratios: NSTX 139047 A_2 (a) and A_4 (b).

affects the width-transport scaling. In Figure 13(a), we show the difference between a prediction for $\Delta_{\mathrm{ped,GCP}}$ using the $\chi_e/D = 3/2$ model and the data from gyrokinetic simulations. At low A values, $\Delta_{\mathrm{ped,GCP}}$ is the same for both $\langle q_e/\Gamma_e\rangle_{\mathrm{ped},3/2}$ and $\langle q_e/\Gamma_e\rangle_{\mathrm{ped,GK}}$, whereas at higher values there is a very large discrepancy. This difference comes from the increased χ_e/D_e value of the KBM for larger A values. We also plot the derivative $\Delta'_{\mathrm{ped,GCP}}$ in Figure 13(b). The quantity $\Delta'_{\mathrm{ped,GCP}}$ has an aspect-ratio dependence — the smaller A, the more sensitive $\Delta_{\mathrm{ped,GCP}}$ is to $\langle q_e/\Gamma_e\rangle_{\mathrm{ped,GK}}$. Writing the derivative of $\Delta_{\mathrm{ped,GCP}}$ in the form of Equation (15) with the diffusivity χ_e/D_e included explicitly,

$$\begin{aligned}\Delta'_{\mathrm{ped,GCP}} &= \frac{d\Delta_{\mathrm{ped,GCP}}}{d\langle q_e/\Gamma_e\rangle_{\mathrm{GCP}}} \\ &= \left(\frac{D_e}{\chi_e}\frac{1}{a_1 D^{\alpha_1}}\right)^{1/(\alpha_1\alpha_2)} \left(\frac{\frac{D_e}{\chi_e}\left(\langle\frac{q_e}{\Gamma_e}\rangle_{\mathrm{ped}} - \frac{3}{2}\right) - d}{a_1\,(D)^{\alpha_1}}\right)^{-1+1/(\alpha_1\alpha_2)},\end{aligned} \tag{18}$$

one sees that increased χ_e/D_e values generally decrease $\Delta_{\mathrm{ped,GCP}}$ and $\Delta'_{\mathrm{ped,GCP}}$.

We comment briefly on the compatibility of width-height scaling, $\Delta_{\mathrm{ped}}(\beta_{\theta,\mathrm{ped}})$, and the width-transport scaling, $\Delta_{\mathrm{ped}}(q_e/\Gamma_e)$. The width-transport scaling in Equations (16) and (17) assumes that $D_e/\chi_e = 3/2$, which is generally a good approximation exactly along the GCP (see Figure 9. However, given that the pedestal experiment may not lie precisely along the GCP [114, 115]), D_e/χ_e for the KBM will likely increase (see Figure 8(a)), changing q_e/Γ_e in this region. Additionally, for simplicity in this work we only consider KBM contributions to q_e/Γ_e. See [19, 35, 113, 116] for pedestal transport models with contributions from various instabilities.

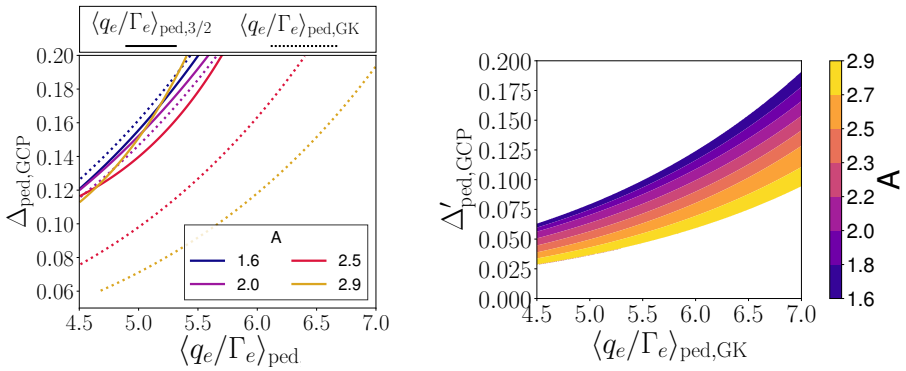

(a) Width versus $\langle q_e/\Gamma_e\rangle_{\mathrm{ped}}$ for model with $\chi_e/D_e = 3/2$ and KBM from gyrokinetic simulations.

(b) Width derivative versus $\langle q_e/\Gamma_e\rangle_{\mathrm{ped,GK}}$ for KBM from gyrokinetic simulations.

Figure 13: Pedestal width (a) and its derivative (b) versus $\langle q_e/\Gamma_e\rangle_{\mathrm{ped}}$ for NSTX 139047 A_2 at fixed $n_{e,\mathrm{ped}}$.

5.5 Radial Dependence

In this section, we describe briefly the radial dependence of gyrokinetic instabilities in pedestal width and height space for NSTX 139047 A_2. We study the 'average' radial location of an instability between $\psi_{1/4} = \psi_{\mathrm{mid}} - \Delta_{\mathrm{ped}}/4$ and $\psi_{3/4} = \psi_{\mathrm{mid}} + \Delta_{\mathrm{ped}}/4$ using the quantity

$$Y = 4\frac{\psi - \psi_{\mathrm{mid}}}{\Delta_{\mathrm{ped}}}, \tag{19}$$

such that $Y_{1/4} = Y(\psi_{1/4}) = -1$ and $Y_{3/4} = Y(\psi_{3/4}) = 1$. Averaging Y for a given mode,

$$\langle Y\rangle_{\mathrm{mode}} \equiv \frac{\sum_{k_y}\int_{-1}^{1} Y\ \mathrm{mode}(Y,k_y)\,dY}{\sum_{k_y,}\int_{-1}^{1} dY}, \tag{20}$$

gives the average Y radial value across the pedestal half-width. Here, mode=1 if the mode is present and mode=0 if not. For example, if KBM were unstable at all radial and $k_y\rho_i$ values then $\langle Y\rangle_{\mathrm{KBM}} = 0$, indicating a uniform radial distribution across the pedestal half-width relative to the pedestal mid-radius.

Figure 14(a) shows that moving along the wide and narrow GCP, initially at small widths the KBM is more common at the pedestal top, but as the pedestal width increases, the KBM is more common around the pedestal foot. This is likely due to the magnetic shear profiles changing as the bootstrap current density increases, shifting the relatively higher magnetic shear (and therefore destabilizing) regions from the pedestal top to the pedestal foot at higher Δ_{ped}, $\beta_{\theta,\mathrm{ped}}$ values. For MTMs in Figure 14(b), the instability is most common near the pedestal top, consistent with other works [31, 117, 118]. Figure 14(c) shows that the TEM only appears in KBM second stability and is also more prevalent

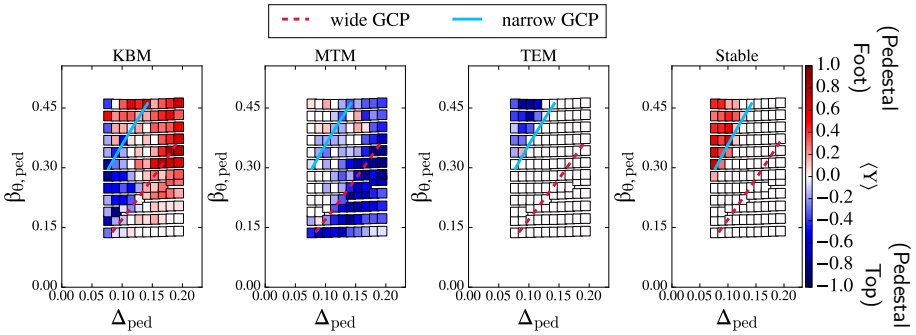

Figure 14: Average radial location $\langle Y \rangle$ defined in Equation (20) of mode type across the pedestal for NSTX 139047 A_2 across wavenumbers $k_y\rho_i \in [0.06, 0.12, 0.18]$.

at the pedestal top, also seen in other works [19, 119]. The lack of TEM instability below the wide GCP branch at lower gradients might result from the relatively narrow $k_y\rho_i \in [0.06, 0.12, 0.18]$ range we include in simulations for this work – because steeper gradients tend to destabilize modes at lower $k_y\rho_i$ values [120, 121], we likely require higher $k_y\rho_i$ values for the pedestals below the wide GCP branch to find TEM instability. Despite the ubiquity of ETG instability in the pedestal [31, 34, 56, 86], we find relatively little dominant ETG modes for $k_y\rho_i \in [0.06, 0.12, 0.18]$, likely because we are again only simulating binormal wavenumbers that are too low. Finally, Figure 14(d) shows that in KBM second stability, much of the pedestal foot is stabilized, which is the only location in $\beta_{\theta,\mathrm{ped}}$, Δ_{ped} space where stabilization occurs for $k_y\rho_i \in [0.06, 0.12, 0.18]$.

6 Flow-Shear Along the Gyrokinetic Critical Pedestal

In this section, we study the efficacy of pedestal flow-shear for two NSTX discharges. The radial shear in plasma rotation Ω_ζ is important in the L-H transition [36, 122, 123] and inter-ELM pedestal dynamics [32, 37, 124–127], where Ω_ζ is the toroidal angular rotation frequency. One key assumption in the EPED model is that flow-shear at the pedestal top suppresses turbulence [8] allowing the pedestal to broaden. We examine this assumption by comparing flow-shear in a standard (139047) and wide (132588) NSTX pedestal along the GCP.

Balancing the radial electric field with the diamagnetic flow [31, 86], we approximate the flow-shear rate $\gamma_E = (r/q)d\Omega_\zeta/dr$ as

$$\gamma_E \approx \frac{r}{q}\frac{\partial}{\partial r}\left(\frac{dp_i}{d\psi}\frac{c}{Z_i e n_i}\right). \tag{21}$$

As a rough estimate of flow-shear efficacy, we compare the flow-shear frequency with the linear drive frequency

$$\omega_{*i} = v_{ti}\sum_s \left(\frac{1}{L_{Ts}} + \frac{1}{L_{ns}}\right), \tag{22}$$

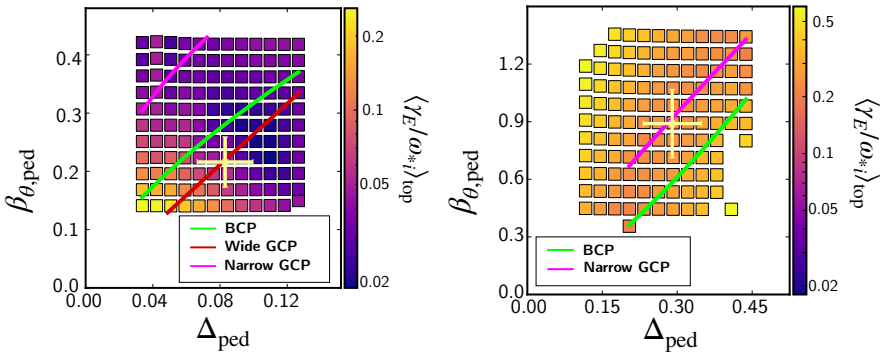

(a) NSTX 139047. (b) NSTX 132588.

Figure 15: Pedestal-top-averaged flow-shear γ_E/ω_{*i} (see Equations (21) to (23)) for NSTX 139047 and 132588, with the BCP, GCP, and equilibrium point (yellow marker).

which is typically comparable to the linear instability growth rate. In Figure 15(a), we plot γ_E/ω_{*i} averaged over the pedestal top,

$$\left\langle \frac{\gamma_E}{\omega_{*i}} \right\rangle_{\mathrm{top}} = (4/\Delta_{\mathrm{ped}}) \int_{\psi_{\mathrm{ped}}}^{\psi_{1/4}} \frac{q_e}{\Gamma_e}\, d\psi, \tag{23}$$

versus pedestal width and height for NSTX 139047. Here, $\psi_{1/4} = \psi_{\mathrm{mid}} - \Delta/4$ and $\psi_{\mathrm{ped}} = \psi_{\mathrm{mid}} - \Delta/2$. At the pedestal top, larger values of $\langle \gamma_E/\omega_{*i} \rangle_{\mathrm{top}}$ suppress turbulence and may facilitate the pedestal's radially inward propagation [8], although too large values may cause other instabilities [128–130]. Moving along the wide GCP and BCP starting from small widths and heights, $\langle \gamma_E/\omega_{*i} \rangle_{\mathrm{top}}$ is a rapidly decreasing function. The marked equilibrium point for NSTX 139047 in Figure 15(a) is at a location where $\langle \gamma_E/\omega_{*i} \rangle_{\mathrm{top}}$ approaches a minimum – moving further along the wide GCP by increasing the width-height may prevent pedestals with insufficient pedestal top flow-shear to increase in pedestal width.

For comparison, we consider pedestal flow-shear for ELM-free wide pedestal NSTX discharge 132588. In Figure 15(b), we plot $\langle \gamma_E/\omega_{*i} \rangle_{\mathrm{top}}$. Compared with NSTX 139047 in Figure 15(a), the wide pedestal has very strong pedestal top flow-shear. This strong flow-shear indicates that this discharge may have sufficient flow-shear to allow the pedestal width to grow to very large values.

We emphasize that using the ratio γ_E/ω_{*i} is only heuristic, and actual gyrokinetic simulations are required to definitively determine flow-shear efficacy across the $\beta_{\theta,\mathrm{ped}}$, Δ_{ped} space. Additionally, given that flow-shear can also affect peeling-ballooning stability [131], determining the effect of pedestal flow-shear on both microstability and macrostability is necessary to understand its role in pedestal evolution.

7 Combined Stability, Flow-Shear, and Transport Constraints

In this section, we discuss the combination of three pedestal constraints discussed in this paper: KBM stability, flow-shear, and transport. Due to its importance as a pedestal growth saturation mechanism, we also heuristically include an ELM constraint [8], but do not calculate it explicitly.

For KBM stability, the Gyrokinetic Critical Pedestal gives the wide and narrow branches, indicated by lines labeled wide GCP and narrow GCP in Figure 16(a). According to kinetic-ballooning-mode stability, the pedestal can only manifest at pressures above the narrow branch and pressures below the wide branch. Arrows in Figure 16(a) along the wide and narrow branches indicate the direction in which the constraint applies, ruling out pedestal access to these excluded regions of $\beta_{\theta,\mathrm{ped}}$ and Δ_{ped}. The grey-shaded regions in Figure 16(a) are KBM-limited.

For flow-shear, we show a single constraint given by $\langle \gamma_E/\omega_{*i} \rangle_{\mathrm{top}}$ in Figure 16(a): values below a critical value indicate that the pedestal top flow-shear is too weak to allow the pedestal to widen. From the results in Section 6 we graph the flow-shear constraint as $\beta_{\theta,\mathrm{ped}} \sim 1/\Delta_{\mathrm{ped}}$. The red-shaded regions Figure 16(a) are shear-limited.

For transport, we plot two constraints in Figure 16(a): $\langle q_e/\Gamma_e \rangle_{\mathrm{ped,lower}}$ and $\langle q_e/\Gamma_e \rangle_{\mathrm{ped,upper}}$, which are the minimum and maximum values of $\langle q_e/\Gamma_e \rangle_{\mathrm{ped}}$ that the particle and heat sources might permit to support a given pedestal profile. In steady state for heat and particle sources P_e and S_e

$$\left\langle \frac{q_e}{\Gamma_e} \right\rangle_{\mathrm{ped}} = \frac{\int P_e dV_{\mathrm{half-width}}}{\int S_e dV_{\mathrm{half-width}}}, \tag{24}$$

where the volume integral is taken over the pedestal half-width. For the example in Figure 16, we assume that pedestal height changes at fixed density

$$\langle \eta_e \rangle_{\mathrm{ped}} \sim \beta_{\theta,\mathrm{ped}}, \tag{25}$$

and hence $\langle q_e/\Gamma_e \rangle_{\mathrm{ped}}$ also increases with $\beta_{\theta,\mathrm{ped}}$ according to Equation (12). If however, η_e were to decrease with $\beta_{\theta,\mathrm{ped}}$, the transport constraints in Figure 16 would change significantly. The blue-shaded regions Figure 16(a) are transport-limited.

Finally, we sketch (but do not explicitly calculate) a peeling-ballooning ELM constraint in Figure 16(a) assuming $\Delta_{\mathrm{ped}} \sim (\beta_{\theta,\mathrm{ped}})^{4/3}$ [8]. Pedestal pressures above the ELM constraint are inaccessible. The orange-shaded regions in Figure 16(a) are ELM-limited.

Figure 16(a) shows that after considering stability, pedestal top flow-shear, and transport, only a relatively narrow window of $\beta_{\theta,\mathrm{ped}}$, Δ_{ped} space may remain for a viable pedestal. In the heuristic example in Figure 16(a), moving along the wide GCP branch, the pedestal growth is eventually stopped by the flow-shear constraint. Moving along the narrow GCP branch, the pedestal growth is stopped by the upper transport constraint.

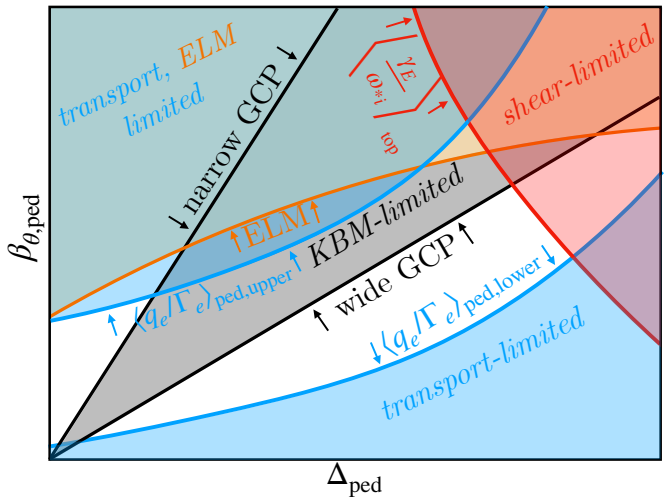

(a) Heuristic constraints.

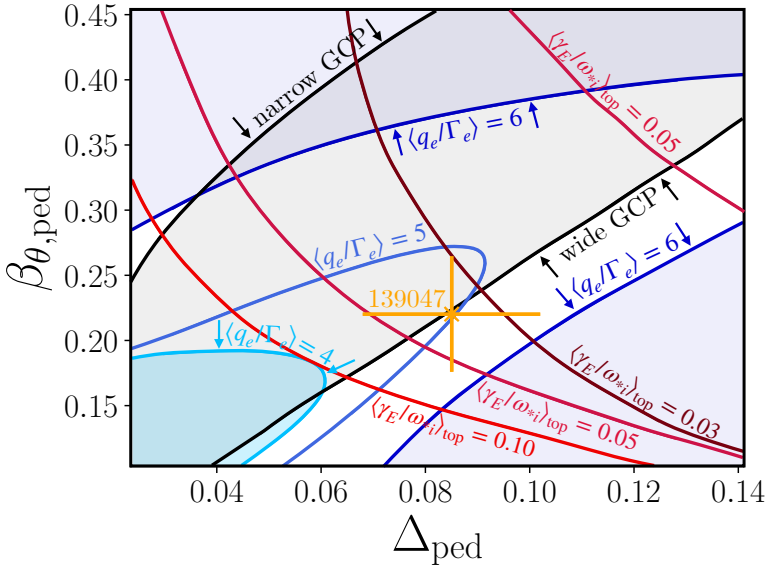

(b) Calculated constraints for NSTX 139047.

Figure 16: Combination of GCP stability, flow-shear, transport, and ELM constraints. Arrows indicate the direction that the constraint acts on in $\beta_{\theta,\mathrm{ped}}$, Δ_{ped} space. Translucent color blocks indicate the excluded regions for a constraint curve of the same color. In (a), accessible pedestal regions are those without any constraints. In this example, for transport constraints $\langle q_e/\Gamma_e\rangle_{\mathrm{ped,lower}}$ and $\langle q_e/\Gamma_e\rangle_{\mathrm{ped,upper}}$, we assume that η_e increases with $\beta_{\theta,\mathrm{ped}}$. In (b), we calculate the constraints in (a) – except for the ELM constraint – for NSTX 139047, with the equilibrium point plotted in orange with 20% uncertainty in $\beta_{\theta,\mathrm{ped}}$, Δ_{ped}.

We now calculate these constraints for an experimental equilibrium, NSTX discharge 139047, which was studied in Section 6. The result is shown in Figure 16(b). For this calculation, the pedestal height was varied at fixed density, so $\langle \eta_e \rangle_{\rm ped} \sim \beta_{\theta,\rm ped}$ in Equation (25) holds. The transport ratio $\langle q_e/\Gamma_e \rangle_{\rm ped}$ has a complex dependence on width and height, which is due to the variation of the transport ratio χ_e/D_e as KBM growth rates decrease. For NSTX 139047, the wide GCP branch generally requires lower values of $\langle q_e/\Gamma_e \rangle_{\rm ped}$ than the narrow branch at fixed pedestal height.

At small $\beta_{\theta,\rm ped}$ (and therefore low $\langle \eta_e \rangle_{\rm ped}$) and large $\Delta_{\rm ped}$ values, the ratio $\langle q_e/\Gamma_e \rangle_{\rm ped} \approx \langle (\chi_e/D_e)\eta_e \rangle_{\rm ped} + 3/2$ increases with *decreasing* $\beta_{\theta,\rm ped}$. This is surprising since the expected scaling is $\langle q_e/\Gamma_e \rangle_{\rm ped} \sim \beta_{\theta,\rm ped}$ (at constant χ_e/D_e). The explanation is that for decreasing $\beta_{\theta,\rm ped}$ values, the ratio χ_e/D_e increases faster than η_e decreases near the wide GCP branch. This is due to χ_e/D_e increasing quickly for KBMs with relatively low growth rates. This is a cautionary result for pedestal transport models that assume that χ_e/D_e does not vary for any given instability.

We also plot contours of constant $\langle \gamma_E/\omega_{*i} \rangle_{\rm top}$ in Figure 16(b). While we have not determined the exact value of $\langle \gamma_E/\omega_{*i} \rangle_{\rm top}$ required for flow-shear to be insufficient for turbulent suppression at the pedestal-top (such an exercise requires a dedicated study), the predicted trend of $\beta_{\theta,\rm ped} \sim 1/\Delta_{\rm ped}$ holds for lower $\Delta_{\rm ped}$, but then reverses for higher $\Delta_{\rm ped}$. This shows that at fixed pedestal height, wide GCP branch pedestals may struggle more to generate sufficient flow-shear than narrow GCP branch pedestals at intermediate values of $\Delta_{\rm ped}$, but at higher $\Delta_{\rm ped}$, the wide GCP branch may be able to access higher flow shear values. The trends of $\langle \gamma_E/\omega_{*i} \rangle_{\rm top}$ increasing at higher $\Delta_{\rm ped}$ for NSTX 139047 and the consistently large $\langle \gamma_E/\omega_{*i} \rangle_{\rm top}$ in the lithiated NSTX discharge 132588 (see Figure 15(b)) may challenge the pessimistic ρ_{*i} flow-shear scaling in [38, 40], but more detailed investigation is required.

We emphasize that our analysis of combined stability, flow-shear, and transport constraints has so far only included a single discharge and that systematic study is needed to determine the generality of the trends shown for NSTX 139047 in Figure 16(b). There are also important caveats the reader should keep in mind. First, our analysis of $\langle q_e/\Gamma_e \rangle_{\rm ped}$ only considered KBM transport ratios from linear gyrokinetic simulations, and much higher fidelity nonlinear simulations are needed to determine the accuracy of our results. Second, our analysis for the flow-shear constraint $\langle \gamma_E/\omega_{*i} \rangle_{\rm top}$ is very low-fidelity, and while we believe may elucidate important trends, systematic higher fidelity analysis is needed to determine its validity.

8 Summary

In this work, we described how a linear gyrokinetic threshold model combined with self-consistent equilibrium variation gives a pedestal width-height scaling expression that depends strongly on aspect-ratio and plasma shaping. These shaping and aspect-ratio scans were performed on an NSTX equilibrium with

self-consistent equilibrium reconstruction. The Gyrokinetic Critical Pedestal scaling for the wide branch kinetic-ballooning-mode pedestals with shaping and aspect-ratio dependence in this NSTX equilibrium is $\Delta_{\rm ped} = 0.92A^{1.04}\kappa^{-1.24}0.38^{\delta}\left(\beta_{\theta,\rm ped}\right)^{1.05}$. It is noteworthy that the width-height scaling has a strong dependence on shaping and aspect-ratio for both the wide and barrow GCP branches [102] — this dependence might not have been reported experimentally due to the relatively narrow range of aspect-ratio, triangularity, and elongation values routinely examined compared with those in the parameter scan in this work. In future work, it is important to study the effect of shaping on both kinetic-ballooning [102] and peeling-ballooning [5, 11, 26, 132] stability to definitively find attractive ELM-free pedestal scenarios.

We demonstrated that whether pedestal height $\beta_{\theta,\rm ped}$ is varied with fixed $n_{e,\rm ped}$ or $T_{e,\rm ped}$ has a big impact on heat and particle transport along the Gyrokinetic Critical Pedestal. In the wide Gyrokinetic Critical Pedestal branch for fixed $n_{e,\rm ped}$ we find that $\Delta_{\rm ped} = 0.028\left(q_e/\Gamma_e - 1.7\right)^{1.5} \sim \left(\eta_e\right)^{1.5}$ and for fixed $T_{e,\rm ped}$ we find $\Delta_{\rm ped} = 0.31\left(q_e/\Gamma_e - 4.7\right)^{0.85} \sim \left(\eta_e\right)^{0.85}$. Thus, during the inter-ELM buildup, not only do relative contributions to $\beta_{\theta,\rm ped}$ from temperature and density have a big effect on the width-height scaling, but also the relative transport through particle and heat channels. While our linear gyrokinetic model has no information about plasma sources, more sophisticated approaches such as transport solvers [133–135] will be sensitive to KBM transport around the Gyrokinetic Critical Pedestal.

In the vicinity of the narrow and wide Gyrokinetic Critical Pedestal branches where KBM becomes marginally stable, the KBM turbulent transport ratios such as χ_e/D_e and χ_e/D_Z vary significantly. This also has implications for reduced transport models in the pedestal [19, 35, 113, 116], given that KBM can produce significant particle and heat flux.

We analyzed the role of flow-shear for two NSTX pedestal discharges, finding that the width and height of an ultra-wide-pedestal ELM-free NSTX discharge had much stronger flow-shear at the pedestal top, possibly permitting its pedestal to grow to a very large width. The regular ELMy NSTX H-mode showed that the flow-shear strength scaled as $1/\Delta_{\rm ped}$ for small to moderate widths [38, 40], but increased with $\Delta_{\rm ped}$ at larger widths. This indicates that the flow-shear can introduce an additional constraint on the pedestal width and height evolution, and might be an important pedestal growth saturation mechanism.

9 Data Availability Statement

Part of the data analysis was performed using the OMFIT integrated modeling framework [61] using the Github projects `gk_ped` [136] and `ideal-ballooning-solver` [68]. The data that support the findings of this study are openly available in Princeton Data Commons at [137].

10 Acknowledgements

We are grateful for conversations with E. A. Belli, J. Candy, S. C. Cowley, D. Dickinson, W. Dorland, R. Maingi, F. I. Parra, M. J. Pueschel, O. Sauter, P. B. Snyder, G. M. Staebler, and H. R. Wilson. This work was supported by the U.S. DoE under contract numbers DE-AC02-09CH11466, DE-SC0022270, DE-SC0022272, and the DoE Early Career Research Program. The US Government retains a non-exclusive, paid-up, irrevocable, world-wide license to publish or reproduce the published form of this manuscript, or allow others to do so, for US Government purposes.

A $\langle \eta_e \rangle_{\rm ped}$

Here we calculate useful expressions for η_e and $\langle \eta_e \rangle_{\rm ped}$. Using new radial coordinates F_{T_e} and F_{n_e},

$$F_{T_e} = 2\frac{\psi - \psi_{\rm mid,T_e}}{\Delta_{{\rm ped},T_e}}, \quad F_{n_e} = 2\frac{\psi - \psi_{\rm mid,n_e}}{\Delta_{{\rm ped},n_e}}, \tag{26}$$

the electron temperature profile is

$$T_e(F_{T_e}) = T_{e0}\left(\tanh(2) - \tanh(F_{T_e})\right) + T_{e,\rm sep}, \tag{27}$$

and the density profile is

$$n_e(F_{n_e}) = n_{e0}\left(\tanh(2) - \tanh(F_{n_e})\right) + n_{e,\rm sep}, \tag{28}$$

which gives an expression for η_e,

$$\eta_e = \frac{L_{n_e}}{L_{T_e}} = \frac{\Delta_{{\rm ped},n_e}}{\Delta_{{\rm ped},T_e}} \frac{\mathrm{sech}(F_{T_e})^2[(n_{e,\rm sep}/n_{e0}) + \tanh(2) - \tanh(F_{n_e})]}{\mathrm{sech}(F_{n_e})^2[(T_{e,\rm sep}/T_{e0}) + \tanh(2) - \tanh(F_{T_e})]}. \tag{29}$$

A.1 Width-Independent Limit

In the limit where $F_{T_e} = F_{n_e} = F$ and $\Delta_{{\rm ped},T_e} = \Delta_{{\rm ped},n_e}$,

$$\eta_e = \frac{[\overline{n} + \tanh(2) - \tanh(F)]}{[\overline{T} + \tanh(2) - \tanh(F)]}, \tag{30}$$

where $\overline{n} = n_{e,\rm sep}/n_{e0}$ and $\overline{T} = T_{e,\rm sep}/T_{e0}$. Averaging η_e over the past half-width gives

$$\begin{aligned}\langle \eta_e \rangle_{\rm ped} = 2\int_{\psi_{\rm mid}-\Delta_{\rm ped}/4}^{\psi_{\rm mid}+\Delta_{\rm ped}/4} \eta_e d\psi/\Delta_{\rm ped} = \int_{F=-1/2}^{F=1/2} \eta_e dF = \\ \frac{\overline{n}(\overline{T}-1) - \overline{T} + 2e^4(\overline{n}\overline{T}-2) + e^8(\overline{n}+\overline{T}+\overline{n}\overline{T}) + (1+e^4)^2(\overline{n}-\overline{T})X}{(\overline{T}(1+e^4)-2)(\overline{T}+e^4(\overline{T}+2))},\end{aligned} \tag{31}$$

where

$$X = \ln \frac{\overline{T} + \tanh(2) - \tanh(1/2)}{\overline{T} + \tanh(2) + \tanh(1/2)}. \quad (32)$$

The quantities η_e and $\langle \eta_e \rangle_{\rm ped}$ in Equations (30) and (31) are independent of the pedestal width.

References

[1] F. Wagner, G. Becker, K. Behringer, et al., "Regime of Improved Confinement and High Beta in Neutral-Beam-Heated Divertor Discharges of the ASDEX Tokamak", Physical Review Letters **49** (1982).

[2] S. M. Kaye, M. G. Bell, K. Bol, et al., "Attainment of high confinement in neutral beam heated divertor discharges in the pdx tokamak", Journal of Nuclear Materials **121** (1984).

[3] M. Shimada, D. J. Campbell, V. Mukhovatov, et al., "Chapter 1: Overview and summary", Nuclear Fusion **47** (2007).

[4] J. E. Kinsey, G. M. Staebler, J. Candy, et al., "Iter predictions using the gyro verified and experimentally validated trapped gyro-landau fluid transport model", Nuclear Fusion **51** (2011).

[5] P. B. Snyder, J. W. Hughes, T. H. Osborne, et al., "High fusion performance in super h-mode experiments on alcator c-mod and diii-d", Nuclear Fusion **59** (2019).

[6] A. J. Creely, M. J. Greenwald, S. B. Ballinger, et al., "Overview of the sparc tokamak", Journal of Plasma Physics **86** (2020).

[7] M. A. Mahdavi, R. Maingi, R. J. Groebner, et al., "Physics of pedestal density profile formation and its impact on H-mode density limit in burning plasmas", Physics of Plasmas **10** (2003).

[8] P. B. Snyder, N. Aiba, M. Beurskens, et al., "Pedestal stability comparison and ITER pedestal prediction", Nuclear Fusion **49** (2009).

[9] P. B. Snyder, R. J. Groebner, J. W. Hughes, et al., "A first-principles predictive model of the pedestal height and width: development, testing and ITER optimization with the EPED model", Nuclear Fusion **51** (2011).

[10] J. R. Walk, P. B. Snyder, J. W. Hughes, et al., "Characterization of the pedestal in Alcator C-Mod ELMing H-modes and comparison with the EPED model", Nuclear Fusion **52** (2012).

[11] P. B. Snyder, W. M. Solomon, K. H. Burrell, et al., "Super H-mode: Theoretical prediction and initial observations of a new high performance regime for tokamak operation", Nuclear Fusion **55** (2015).

[12] J. W. Hughes, P. B. Snyder, M. L. Reinke, et al., "Access to pedestal pressure relevant to burning plasmas on the high magnetic field tokamak alcator c-mod", Nuclear Fusion **58** (2018).

[13] A. Diallo, J. Canik, T. Göerler, et al., "Progress in characterization of the pedestal stability and turbulence during the edge-localized-mode cycle on national spherical torus experiment", Nuclear Fusion **53** (2013).

[14] S. Saarelma, C. D. Challis, L. Garzotti, et al., "Integrated modelling of H-mode pedestal and confinement in JET-ILW", Plasma Physics and Controlled Fusion **60** (2017).

[15] J. W. Connor, R. J. Hastie, and J. B. Taylor, "High mode number stability of an axisymmetric toroidal plasma", Proc R Soc London Ser A **365** (1979).

[16] E. Wang, X. Xu, J. Candy, et al., "Linear gyrokinetic analysis of a DIII-D H-mode pedestal near the ideal ballooning threshold", Nuclear Fusion **52** (2012).

[17] P. B. Snyder, H. R. Wilson, J. R. Ferron, et al., "Edge localized modes and the pedestal: A model based on coupled peeling–ballooning modes", Physics of Plasmas **9** (2002).

[18] J. W. Hughes, N. T. Howard, P. Rodriguez-Fernandez, et al., "Projections of H-mode access and edge pedestal in the SPARC tokamak", Journal of Plasma Physics **86** (2020).

[19] W. Guttenfelder, R. J. Groebner, J. M. Canik, et al., "Testing predictions of electron scale turbulent pedestal transport in two DIII-D ELMy H-modes", Nuclear Fusion **61** (2021).

[20] W. Suttrop, O. Gruber, B. Kurzan, et al., "Effect of plasma shape variation on elms and h-mode pedestal properties in asdex upgrade", Plasma Physics and Controlled Fusion **42** (2000).

[21] T. H. Osborne, J. R. Ferron, R. J. Groebner, et al., "The effect of plasma shape on h-mode pedestal characteristics on diii-d", Plasma Physics and Controlled Fusion **42** (2000).

[22] J. R. Ferron, M. S. Chu, G. L. Jackson, et al., "Modification of high mode pedestal instabilities in the diii-d tokamak", Physics of Plasmas **7** (2000).

[23] L. Lao, Y Kamada, T Oikawa, et al., "Dependence of edge stability on plasma shape and local pressure gradients in the diii-d and jt-60u tokamaks", Nuclear fusion **41** (2001).

[24] A. W. Leonard, T. A. Casper, R. J. Groebner, et al., "Pedestal performance dependence upon plasma shape in diii-d", in, Vol. 47 (2007).

[25] A. Nelson, L. Schmitz, C. Paz-Soldan, et al., "Robust avoidance of edge-localized modes alongside gradient formation in the negative triangularity tokamak edge robust avoidance of edge-localized modes alongside gradient formation in the negative triangularity tokamak edge", Physical Review Letters (2023).

[26] A. Merle, O. Sauter, and S. Y. Medvedev, "Pedestal properties of h-modes with negative triangularity using the eped-ch model", Plasma Physics and Controlled Fusion **59** (2017).

[27] Y. K. Peng and D. J. Strickler, "Features of spherical torus plasmas", Nuclear Fusion **26** (1986).

[28] J. Parisi, W. Guttenfelder, O. Nelson, et al., "Kinetic-ballooning-limited pedestals in spherical tokamak plasmas", Nuclear Fusion **64** (2024).

[29] S. C. Cowley, R. M. Kulsrud, and R. Sudan, "Considerations of ion temperature gradient driven turbulence", Physics of Fluids B: Plasma Physics **3** (1991).

[30] F. Jenko, W. Dorland, and G. W. Hammett, "Critical gradient formula for toroidal electron temperature gradient modes", Physics of Plasmas **8** (2001).

[31] D. R. Hatch, M. Kotschenreuther, S. Mahajan, et al., "Microtearing turbulence limiting the JET-ILW pedestal", Nuclear Fusion **56** (2016).

[32] D. R. Hatch, M. Kotschenreuther, S. Mahajan, et al., "A gyrokinetic perspective on the JET-ILW pedestal", Nuclear Fusion **57** (2017).

[33] R. M. Churchill, C. S. Chang, S. Ku, et al., "Pedestal and edge electrostatic turbulence characteristics from an XGC1 gyrokinetic simulation", Plasma Physics and Controlled Fusion **59** (2017).

[34] B. Chapman-Oplopoiou, D. Hatch, A. Field, et al., "The role of etg modes in jet–ilw pedestals with varying levels of power and fuelling", Nuclear Fusion **62** (2022).

[35] A. R. Field, B. Chapman-Oplopoiou, J. W. Connor, et al., "Comparing pedestal structure in jet-ilw h-mode plasmas with a model for stiff etg turbulent heat transport", Philosophical Transactions of the Royal Society A: Mathematical, Physical and Engineering Sciences **381** (2023).

[36] R. J. Groebner, K. H. Burrell, and R. P. Seraydarian, "Role of edge electric field and poloidal rotation in the l-h transition", Physical Review Letters **64** (1990).

[37] J Schirmer, G. Conway, H Zohm, et al., "The radial electric field and its associated shear in the asdex upgrade tokamak", Nuclear Fusion **46** (2006).

[38] M. Kotschenreuther, D. R. Hatch, S. Mahajan, et al., "Pedestal transport in H-mode plasmas for fusion gain", Nuclear Fusion **57** (2017).

[39] M. Kotschenreuther, X. Liu, S. M. Mahajan, et al., *Transport barriers in magnetized plasmas – general theory with dynamical constraints (https://arxiv.org/abs/2310.17107)*, 2023.

[40] M. Kotschenreuther, W. Dorland, Q. P. Liu, et al., "First principles calculations of tokamak energy transport", in Proceedings of the 16th international fusion energy conference, montreal, canada (1996).

[41] M. N. Beurskens, T. H. Osborne, L. D. Horton, et al., "Pedestal width and elm size identity studies in jet and diii-d; implications for iter", Plasma Physics and Controlled Fusion **51** (2009).

[42] M. N. Beurskens, T. H. Osborne, P. A. Schneider, et al., "H-mode pedestal scaling in diii-d, asdex upgrade, and jet", Physics of Plasmas **18** (2011).

[43] C. Pan, G. M. Staebler, L. L. Lao, et al., "Investigation of energy transport in diii-d high-β_P east-demonstration discharges with the tglf turbulent and neo neoclassical transport models", Nuclear Fusion **57** (2017).

[44] S. Ding, X. Jian, A. M. Garofalo, et al., "The dominant micro-turbulence instabilities in the lower q_{95} high β_p plasmas on diii-d and predict-first extrapolation", Nuclear Fusion **60** (2020).

[45] G. W. Hammett and F. W. Perkins, "Fluid moment models for landau damping with application to the ion-temperature-gradient instability", Physical Review Letters **64** (1990).

[46] M. Romanelli, C. Bourdelle, and W. Dorland, "Effects of high density peaking and high collisionality on the stabilization of the electrostatic turbulence in the frascati tokamak upgrade", Physics of Plasmas **11** (2004).

[47] Y Ren, S. M. Kaye, E Mazzucato, et al., "Density gradient stabilization of electron temperature gradient driven turbulence in a spherical tokamak.", Physical review letters **106** (2011).

[48] M. A. Beer, G. W. Hammett, G. Rewoldt, et al., "Gyrofluid simulations of turbulence suppression in reversed-shear experiments on the tokamak fusion test reactor", in, Vol. 4 (1997).

[49] C. Bourdelle, G. T. Hoang, X. Litaudon, et al., "Impact of the a parameter on the microstability of internal transport barriers", Nuclear Fusion **45** (2005).

[50] J. McClenaghan, A. Garofalo, G. Staebler, et al., "Shafranov shift bifurcation of turbulent transport in the high β_p scenario on diii-d", Nuclear Fusion **59** (2019).

[51] H. Meyer, T. Eich, M. Beurskens, et al., "Overview of progress in european medium sized tokamaks towards an integrated plasma-edge/wall solution", Nuclear Fusion **57** (2017).

[52] P. Rodriguez-Fernandez, N. T. Howard, and J. Candy, "Nonlinear gyrokinetic predictions of sparc burning plasma profiles enabled by surrogate modeling", Nuclear Fusion **62** (2022).

[53] S. Saarelma, J. W. Connor, P. Bilkova, et al., "Testing a prediction model for the h-mode density pedestal against jet-ilw pedestals", Nuclear Fusion **63** (2023).

[54] S. Baalrud, N. Ferraro, L. Garrison, et al., *A community plan for fusion energy and discovery plasma sciences*, 2020.

[55] R. J. Groebner, M. A. Mahdavi, A. W. Leonard, et al., "The role of neutrals in high-mode (h-mode) pedestal formation", Physics of Plasmas **9** (2002).

[56] M. Kotschenreuther, X. Liu, D. R. Hatch, et al., "Gyrokinetic analysis and simulation of pedestals to identify the culprits for energy losses using 'fingerprints'", Nuclear Fusion **59** (2019).

[57] S. Mordijck, "Overview of density pedestal structure: role of fueling versus transport", Nuclear Fusion **60** (2020).

[58] A. Kit, A. E. Järvinen, L. Frassinetti, et al., "Supervised learning approaches to modeling pedestal density", Plasma Physics and Controlled Fusion **65** (2023).

[59] L. Horvath, B. Lomanowski, J. Karhunen, et al., "Pedestal particle balance studies in jet-ilw h-mode plasmas", Plasma Physics and Controlled Fusion **65** (2023).

[60] R. Maingi, R. E. Bell, J. M. Canik, et al., "Triggered confinement enhancement and pedestal expansion in high-confinement-mode discharges in the national spherical torus experiment", Physical Review Letters **105** (2010).

[61] O. Meneghini, S. Smith, L. Lao, et al., "Integrated modeling applications for tokamak experiments with omfit", Nuclear Fusion **55** (2015).

[62] L. L. Lao, S. Kruger, C. Akcay, et al., "Application of machine learning and artificial intelligence to extend efit equilibrium reconstruction", Plasma Physics and Controlled Fusion **64** (2022).

[63] L. C. Appel, G. T. Huysmans, L. L. Lao, et al., "A unified approach to equilibrium reconstruction", in, Vol. 2 (33rd EPS Conference on Plasma Physics 2006, EPS 2006, 2006).

[64] W. Dorland, F. Jenko, M. Kotschenreuther, et al., "Electron temperature gradient turbulence", Physical Review Letters **85** (2000).

[65] M. Barnes, D. Dickinson, W Dorland, et al., *Gs2 v8.1.0 (8.1.0)*, technical report (Zenodo, 2021).

[66] J. Candy, E. Belli, and R. Bravenec, "A high-accuracy eulerian gyrokinetic solver for collisional plasmas", Journal of Computational Physics **324** (2016).

[67] R. L. Miller, Y. R. Lin-Liu, A. D. Turnbull, et al., "Stable equilibria for bootstrap-current-driven low aspect ratio tokamaks", Physics of Plasmas **4** (1997).

[68] R. Gaur, *Ideal-ballooning-solver*, `https://github.com/rahulgaur104/ideal-ballooning-solver/`, 2023.

[69] O. Sauter, C. Angioni, and Y. R. Lin-Liu, "Neoclassical conductivity and bootstrap current formulas for general axisymmetric equilibria and arbitrary collisionality regime", Physics of Plasmas **6** (1999).

[70] A. Redl, C. Angioni, E. Belli, et al., "A new set of analytical formulae for the computation of the bootstrap current and the neoclassical conductivity in tokamaks", Physics of Plasmas **28** (2021).

[71] S. F. Smith, A. Kirk, B. Chapman-Oplopoiou, et al., "Pedestal analysis of MAST ELMy regimes", Plasma Physics and Controlled Fusion **64** (2022).

[72] P. J. Catto, "Linearized gyro-kinetics", Plasma Physics **20** (1978).

[73] E. A. Frieman and L. Chen, "Nonlinear gyrokinetic equations for low-frequency electromagnetic waves in general plasma equilibria", The Physics of Fluids **25** (1982).

[74] F. I. Parra and P. J. Catto, "Limitations of gyrokinetics on transport time scales", Plasma Physics and Controlled Fusion **50** (2008).

[75] I. G. Abel, G. G. Plunk, E. Wang, et al., "Multiscale gyrokinetics for rotating tokamak plasmas: fluctuations, transport and energy flows", Reports on Progress in Physics **76** (2013).

[76] R. Gaur, S. Buller, M. E. Ruth, et al., *An adjoint-based method for optimizing mhd equilibria against the infinite-n, ideal ballooning mode (https://arxiv.org/abs/2302.07673)*, 2023.

[77] W. M. Tang, J. W. Connor, and R. J. Hastie, "Kinetic-ballooning-mode theory in general geometry", Nuclear Fusion **20** (1980).

[78] K. Aleynikova, A. Zocco, P. Xanthopoulos, et al., "Kinetic ballooning modes in tokamaks and stellarators", Journal of Plasma Physics **84** (2018).

[79] D. R. Ernst, P. T. Bonoli, P. J. Catto, et al., "Role of trapped electron mode turbulence in internal transport barrier control in the Alcator C-Mod Tokamak", Physics of Plasmas **11** (2004).

[80] D. R. Hatch, D. Told, F. Jenko, et al., "Gyrokinetic study of ASDEX Upgrade inter-ELM pedestal profile evolution", Nuclear Fusion **55** (2015).

[81] C. F. Clauser, W. Guttenfelder, T. Rafiq, et al., "Linear ion-scale microstability analysis of high and low-collisionality nstx discharges and nstx-u projections", Physics of Plasmas **29** (2022).

[82] J. F. Drake, N. T. Gladd, C. S. Liu, et al., "Microtearing modes and anomalous transport in tokamaks", Physical Review Letters **44** (1980).

[83] J. W. Connor, S. C. Cowley, and R. J. Hastie, "Micro-tearing stability in tokamaks", Plasma Physics and Controlled Fusion **32** (1990).

[84] D. R. Hatch, M. Kotschenreuther, S. M. Mahajan, et al., "Microtearing modes as the source of magnetic fluctuations in the JET pedestal", Nuclear Fusion **61** (2021).

[85] M. R. Hardman, F. I. Parra, C. Chong, et al., "Extended electron tails in electrostatic microinstabilities and the nonadiabatic response of passing electrons", Plasma Physics and Controlled Fusion **64** (2022).

[86] J. F. Parisi, F. I. Parra, C. M. Roach, et al., "Toroidal and slab ETG instability dominance in the linear spectrum of JET-ILW pedestals", Nuclear Fusion **60** (2020).

[87] T. Adkins, A. A. Schekochihin, P. G. Ivanov, et al., "Electromagnetic instabilities and plasma turbulence driven by electron-temperature gradient", Journal of Plasma Physics **88** (2022).

[88] A. Zocco, N. F. Loureiro, D. Dickinson, et al., "Kinetic microtearing modes and reconnecting modes in strongly magnetised slab plasmas", Plasma Physics and Controlled Fusion **57** (2015).

[89] L. I. Rudakov and R. Z. Sagdeev, "On the instability of a nonuniform rarefied plasma in a strong magnetic field", Soviet Physics Doklady **6** (1961).

[90] M. Nunami, T. H. Watanabe, H. Sugama, et al., "Linear gyrokinetic analyses of itg modes and zonal flows in lhd with high ion temperature", Plasma and Fusion Research **6** (2011).

[91] D. R. Hatch, M. J. Pueschel, F. Jenko, et al., "Origin of magnetic stochasticity and transport in plasma microturbulence", Physical Review Letters **108** (2012).

[92] D. Kennedy, M. Giacomin, F. Casson, et al., "Electromagnetic gyrokinetic instabilities in step", Nuclear Fusion **63** (2023).

[93] D. Told, F. Jenko, P. Xanthopoulos, et al., "Gyrokinetic microinstabilities in ASDEX Upgrade edge plasmas", Physics of Plasmas **15** (2008).

[94] C. Angioni, P. T. Lang, and P. Manas, "Density gradient driven microinstabilities and turbulence in asdex upgrade pellet fuelled plasmas", Nuclear Fusion **57** (2017).

[95] D. R. Hatch, M. Kotschenreuther, S. M. Mahajan, et al., "Direct Gyrokinetic Comparison of Pedestal Transport in JET with Carbon and ITER-Like Walls", Nuclear Fusion **59** (2019).

[96] M. R. Hardman, F. I. Parra, B. S. Patel, et al., "New linear stability parameter to describe low-beta electromagnetic microinstabilities driven by passing electrons in axisymmetric toroidal geometry", Plasma Physics and Controlled Fusion **65** (2023).

[97] L. Leppin, T. Görler, M. Cavedon, et al., "Complex structure of turbulence across the asdex upgrade pedestal", Journal of Plasma Physics **89** (2023).

[98] R. J. Groebner, P. B. Snyder, T. H. Osborne, et al., "Limits to the h-mode pedestal pressure gradient in diii-d", Nuclear Fusion **50** (2010).

[99] W. Wan, S. E. Parker, Y. Chen, et al., "Global Gyrokinetic Simulation of Tokamak Edge Pedestal Instabilities", Physical Review Letters **109** (2012).

[100] J. Hughes, P. Snyder, J. Walk, et al., "Pedestal structure and stability in h-mode and i-mode: a comparative study on alcator c-mod", Nuclear Fusion **53** (2013).

[101] G. F. Harrer, M. Faitsch, L. Radovanovic, et al., "Quasicontinuous exhaust scenario for a fusion reactor: the renaissance of small edge localized modes", Physical Review Letters **129** (2022).

[102] J. F. Parisi, A. O. Nelson, R. Gaur, et al., "Kinetic-ballooning-bifurcation in tokamak pedestals across shaping and aspect-ratio", Physics of Plasmas **31** (2024).

[103] J. W. Berkery, P. O. Adebayo-Ige, H. A. Khawaldeh, et al., "Nstx-u research advancing the physics of spherical tokamaks", Nuclear Fusion (2024).

[104] R. Maingi, J. M. Canik, R. E. Bell, et al., "Effect of progressively increasing lithium conditioning on edge transport and stability in high triangularity NSTX H-modes", Fusion Engineering and Design **117** (2017).

[105] B. A. Grierson, X. Yuan, M. Gorelenkova, et al., "Orchestrating transp simulations for interpretative and predictive tokamak modeling with omfit", Fusion Science and Technology **74** (2018).

[106] J. E. Menard, *Next-step low-aspect-ratio tokamak design studies*, IAEA-FEC P/8 2215, 2023.

[107] R. Maingi, T. H. Osborne, M. G. Bell, et al., "Dependence of recycling and edge profiles on lithium evaporation in high triangularity, high performance NSTX H-mode discharges", Journal of Nuclear Materials **463** (2015).

[108] T. C. Luce, "An analytic functional form for characterization and generation of axisymmetric plasma boundaries", Plasma Physics and Controlled Fusion **55** (2013).

[109] G. F. Matthews, M. Beurskens, S. Brezinsek, et al., "Jet iter-like wall - overview and experimental programme", Physica Scripta T **T145** (2011).

[110] J. L. Luxon, "A design retrospective of the diii-d tokamak", Nuclear Fusion **42** (2002).

[111] J. E. Menard, T. Brown, L. El-Guebaly, et al., "Fusion nuclear science facilities and pilot plants based on the spherical tokamak", Nuclear Fusion **56** (2016).

[112] M. J. Pueschel, M. Kammerer, and F. Jenko, "Gyrokinetic turbulence simulations at high plasma beta", Physics of Plasmas **15** (2008).

[113] D. R. Hatch, M. Kotschenreuther, P. Li, et al., "Modeling electron temperature profiles in the pedestal with simple formulas for etg transport", Nuclear Fusion (2024).

[114] W. Guttenfelder, D. Battaglia, A. Diallo, et al., "Gyrokinetic prediction of microstability and transport in nstx h-mode pedestals", in Aps division of plasma physics meeting abstracts, Vol. 2021, APS Meeting Abstracts (Jan. 2021).

[115] J. Dominski, W. Guttenfelder, D. Hatch, et al., "Global micro-tearing modes in the wide pedestal of an NSTX plasma", Physics of Plasmas **31** (2024).

[116] D. R. Hatch, C. Michoski, D. Kuang, et al., "Reduced models for ETG transport in the tokamak pedestal", Physics of Plasmas **29** (2022).

[117] D. Dickinson, C. M. Roach, S. Saarelma, et al., "Kinetic Instabilities that Limit β in the Edge of a Tokamak Plasma: A Picture of an H - Mode Pedestal", Physical Review Letters **108** (2012).

[118] D. Dickinson, C. M. Roach, S. Saarelma, et al., "Microtearing modes at the top of the pedestal", Plasma Physics and Controlled Fusion **55** (2013).

[119] D. P. Fulton, Z. Lin, I. Holod, et al., "Microturbulence in DIII-D tokamak pedestal. I. Electrostatic instabilities", Physics of Plasmas **21** (2014).

[120] M. Barnes, F. I. Parra, and A. A. Schekochihin, "Critically balanced ion temperature gradient turbulence in fusion plasmas", Physical Review Letters **107** (2011).

[121] J. F. Parisi, F. I. Parra, C. M. Roach, et al., "Three-dimensional inhomogeneity of electron-temperature-gradient turbulence in the edge of tokamak plasmas", Nuclear Fusion **62** (2022).

[122] B. N. Rogers, J. F. Drake, and A. Zeiler, "Phase Space of Tokamak Edge Turbulence, the L-H Transition, and the Formation of the Edge Pedestal", Physical Review Letters **81** (1998).

[123] M. Cavedon, G. Birkenmeier, T. Pütterich, et al., "Connecting the global h-mode power threshold to the local radial electric field at asdex upgrade", Nuclear Fusion **60** (2020).

[124] P. B. Snyder, K. H. Burrell, H. R. Wilson, et al., "Stability and dynamics of the edge pedestal in the low collisionality regime: physics mechanisms for steady-state elm-free operation", Nuclear Fusion **47** (2007).

[125] Z. Yan, G. R. McKee, R. J. Groebner, et al., "High-frequency coherent edge fluctuations in a high-pedestal-pressure quiescent H-mode plasma", Physical Review Letters **107** (2011).

[126] X. Chen, K. H. Burrell, T. H. Osborne, et al., "Bifurcation of quiescent h-mode to a wide pedestal regime in diii-d and advances in the understanding of edge harmonic oscillations", Nuclear Fusion **57** (2017).

[127] K. Barada, T. L. Rhodes, K. H. Burrell, et al., "Quasistationary plasma predator-prey system of coupled turbulence, drive, and sheared e×b flow during high performance diii-d tokamak discharges", Physical Review Letters **120** (2018).

[128] P. J. Catto, M. N. Rosenbluth, and C. S. Liu, "Parallel velocity shear instabilities in an inhomogeneous plasma with a sheared magnetic field", The Physics of Fluids **16** (1973).

[129] S. L. Newton, S. C. Cowley, and N. F. Loureiro, "Understanding the effect of sheared flow on microinstabilities", Plasma Physics and Controlled Fusion **52** (2010).

[130] A. A. Schekochihin, E. G. Highcock, and S. C. Cowley, "Subcritical fluctuations and suppression of turbulence in differentially rotating gyrokinetic plasmas", Plasma Physics and Controlled Fusion **54** (2012).

[131] P. W. Xi, X. Q. Xu, X. G. Wang, et al., "Influence of equilibrium shear flow on peeling-ballooning instability and edge localized mode crash", Physics of Plasmas **19** (2012).

[132] A. Y. Pankin, T. Rafiq, A. H. Kritz, et al., "Investigation of the plasma shaping effects on the h-mode pedestal structure using coupled kinetic neoclassical/mhd stability simulations", Physics of Plasmas **24** (2017).

[133] J. Candy, C. Holland, R. E. Waltz, et al., "Tokamak profile prediction using direct gyrokinetic and neoclassical simulation", Physics of Plasmas **16** (2009).

[134] M. Barnes, I. G. Abel, W. Dorland, et al., "Direct multiscale coupling of a transport code to gyrokinetic turbulence codes", Physics of Plasmas **17** (2010).

[135] A. D. Siena, A. B. Navarro, T. Luda, et al., "Global gyrokinetic simulations of asdex upgrade up to the transport timescale with gene-tango", Nuclear Fusion **62** (2022).

[136] J. F. Parisi, A. O. Nelson, and R. Gaur, *Gk_ped*, `https://github.com/gafusion/OMFIT-source/tree/gk_ped`, 2023.

[137] J. F. Parisi, *Data for 'Stability and Transport of Gyrokinetic Critical Pedestals'*, (2024) `10.34770/4mdp-8z16`.